JGR Planets

RESEARCH ARTICLE
10.1029/2019JE006298

Special Section:
Investigations of Vera Rubin Ridge, Gale Crater

Regional Structural Orientation of the Mount Sharp Group Revealed by In Situ Dip Measurements and Stratigraphic Correlations on the Vera Rubin Ridge

Nathaniel T. Stein[1], Daven P. Quinn[2], John P. Grotzinger[1], Christopher Fedo[3], Bethany L. Ehlmann[1,4], Kathryn M. Stack[4], Lauren A. Edgar[5], Abigail A. Fraeman[4], and Robert Deen[4]

[1]Division of Geological and Planetary Sciences, California Institute of Technology, Pasadena, CA, USA, [2]Department of Geoscience, University of Wisconsin-Madison, Madison, WI, USA, [3]Department of Earth and Planetary Sciences, University of Tennessee, Knoxville, Knoxville, TN, USA, [4]Jet Propulsion Laboratory, California Institute of Technology, Pasadena, CA, USA, [5]Astrogeology Science Center, U.S. Geological Survey, Flagstaff, AZ, USA

Abstract Ground-based bedding orientation measurements are critical to determine the geologic history and processes of sedimentation in Gale crater, Mars. We constrain the dip of lacustrine strata of the Blunts Point, Pettegrove Point, and Jura members of the Murray formation using a combination of regional stratigraphic correlations and bed attitude measurements from stereo Mastcam images taken by the Mars Science Laboratory Curiosity rover. In situ bed attitude measurements using a principal component analysis-based regression method reveal a wide range of dips and dip azimuths owing to a combination of high stereo errors, postdepositional deformation of strata (e.g., fracturing, rotation, and impact cratering), and different primary depositional dips. These constrain regional dips to be within several degrees of horizontal on average. Stratigraphic correlations between targets observed in the Glen Torridon trough and at the Pettegrove Point-Jura member contact of Vera Rubin ridge (VRR) constrain dips to be between 3°SE and 2°NW, consistent with nearly flat strata deposited horizontally on an equipotential surface. The Jura member is determined to be stratigraphically equivalent to the northern portion of the Glen Torridon trough. Rover-based dip magnitudes are generally significantly shallower than the orientation of VRR member contacts measured from High Resolution Imaging Science Experiment-based traces, suggesting the sedimentary strata and VRR member contacts may be discordant.

Plain Language Summary The orientation of sedimentary strata is one of the most fundamental measurements of structural geology because it records information about the processes of deposition and subsequent deformation of those strata. For the last 7 years, the Curiosity rover has traversed predominantly fluviolacustrine (river- and lake-deposited) strata. Recently, the rover traversed the Vera Rubin ridge (VRR), a topographic rise within a larger collection of strata with rock exposures whose orientation can be measured using overlapping (stereo) images taken by cameras aboard the rover. By measuring the orientation of beds in stereo rover images and comparing the elevation of similar rock lithologies found along the traverse, we constrain the strata that comprise the VRR to be horizontal or only shallowly dipping. This result is consistent with the sediment that formed the VRR being deposited on a nearly horizontal surface, suggesting that at least the strata that make up the lower portion of Mount Sharp, the large sedimentary mound in Gale crater that dips more steeply outward, may not have directly contributed to its primary formation. The near-flat orientation also indicates that some portion of the VRR occurs at the same elevation as the region south of the ridge called Glen Torridon.

Key Points:
- We use stereo rover images and stratigraphic correlations to constrain the dip of Vera Rubin ridge strata to be flat or nearly flat
- The Jura member of the Vera Rubin ridge is stratigraphically equivalent to part of Glen Torridon
- Vera Rubin ridge member contacts and the strata that comprise them are likely discordant

Supporting Information:
- Supporting Information S1
- Table S1

Correspondence to:
N. T. Stein,
nstein@caltech.edu

Citation:
Stein, N. T., Quinn, D. P., Grotzinger, J. P., Fedo, C., Ehlmann, B. L., Stack, K. M., et al. (2020). Regional structural orientation of the Mount Sharp group revealed by in situ dip measurements and stratigraphic correlations on the Vera Rubin ridge. *Journal of Geophysical Research: Planets*, *125*, e2019JE006298. https://doi.org/10.1029/2019JE006298

Received 2 DEC 2019
Accepted 25 MAR 2020
Accepted article online 13 APR 2020

Author Contributions:
Conceptualization: Nathaniel T. Stein, John P. Grotzinger
Data curation: Nathaniel T. Stein, Robert Deen
Formal analysis: Nathaniel T. Stein, Daven P. Quinn, Christopher Fedo, Kathryn M. Stack, Lauren A. Edgar
Investigation: Nathaniel T. Stein
(continued)

1. Introduction

The orientation of sedimentary strata records information about their processes of deposition and subsequent deformation and is one of the most fundamental measurements of structural geology. In Gale crater, Mars, stereo images collected by the Mars Science Laboratory (MSL) Curiosity rover permit quantification of bedding attitudes of outcrops exposed along the rover's traverse. These measurements are useful for establishing sediment transport directions recorded by cross bedding, revealing patterns of deformation, and

Methodology: Nathaniel T. Stein, Daven P. Quinn, John P. Grotzinger, Christopher Fedo, Bethany L. Ehlmann, Kathryn M. Stack
Resources: John P. Grotzinger
Software: Nathaniel T. Stein, Daven P. Quinn
Supervision: John P. Grotzinger
Validation: Nathaniel T. Stein, Daven P. Quinn
Visualization: Nathaniel T. Stein, Daven P. Quinn, Bethany L. Ehlmann, Kathryn M. Stack
Writing - original draft: Nathaniel T. Stein
Writing – review & editing: Nathaniel T. Stein, Daven P. Quinn, John P. Grotzinger, Christopher Fedo, Bethany L. Ehlmann, Kathryn M. Stack, Lauren A. Edgar, Abigail A. Fraeman, Robert Deen

creating the basis for regional stratigraphic correlation. Collectively, ground-based bedding orientation measurements are critical to determine the history and processes of sedimentation and deformation in Gale crater.

On Earth, bedding orientation measurements are frequently made in situ using a geological compass. On Mars, attitudes must be measured using remotely sensed data consisting of at least one image and a corresponding digital elevation model (DEM). Numerous studies have pursued bedding orientations, particularly dips, using orbital mapping of layered rocks on Mars (e.g., DiBiase et al., 2013; Fraeman et al., 2013; Fueten et al., 2005; Goudge et al., 2017; Hynek & Phillips, 2008; Kite et al., 2013, 2016; Le Deit et al., 2013; Lewis & Aharonson, 2006, 2014; Lewis, Aharonson, Grotzinger, Kirk, et al., 2008; Metz et al., 2010; Milliken et al., 2010; Okubo, 2010; Okubo et al., 2008; Quinn & Ehlmann, 2019a, 2019b; Stack et al., 2013). Orbiter-based dip measurements are constrained by resolution to layered deposits that often extend for hundreds to thousands of meters, whereas bedding orientation estimates or measurements at the centimeter to meter scale are possible using rover-based stereo images (e.g., Arvidson et al., 2011; Barnes et al., 2018; Banham et al., 2018; Hayes et al., 2011; Lewis, Aharonson, Grozinger, Squyres, et al., 2008; Lewis & Turner, 2019; Lewis et al., 2020; Squyres et al., 2004; Turner & Lewis, 2019; Watters et al., 2011).

Prior to Curiosity's arrival at Vera Rubin ridge (VRR), structural orientation measurements of inferred fluviolacustrine strata along the traverse were restricted primarily to visual assessments of dip directions (i.e., azimuths) (e.g., Grotzinger et al., 2015) due to the limited extent of outcrops. Most quantified rover image-based structural orientation measurements reported to date have been made in the Stimson formation (Banham et al., 2018) and more recently in the Murray formation in VRR and Glen Torridon (Lewis & Turner, 2019; Turner & Lewis, 2019). The resistant strata that comprise VRR (defined in section 2), first encountered on Sol 1809, are the first beds within the Murray formation with sufficient exposure to measure numerous attitudes from stereo Mastcam images over a wide region. These strata were also investigated earlier from orbit (Fraeman et al., 2013), making them the first to be independently assessed in situ following orbiter-based predictions. The relationship between VRR and adjacent units was unclear from orbital data (Fraeman et al., 2016; Stack et al., 2017) prior to Curiosity's in situ investigation of the ridge. Hence, a major motivation for measuring the bedding orientation of VRR strata is to place it in stratigraphic context with the rest of the Mount Sharp group.

Another key motivation for quantifying the bedding orientation of strata in the Mount Sharp group is to constrain hypotheses regarding the origin of Mount sharp and other large sedimentary mounds in Martian craters, a significant problem in sedimentary geology that is likely unique to Mars (Grotzinger & Milliken, 2012; Kite et al., 2016). As described in Kite et al. (2016), mechanisms for mound formation generally invoke either (1) flat-lying or shallowly dipping strata that eroded to their present morphology (Andrews-Hanna et al., 2010; Day & Kocurek, 2016; Kite et al., 2013; Malin & Edgett, 2000) or (2) deposition of sediment on preexisting topography that grew mounds in place (Kite et al., 2013, 2016). The latter scenario, also called anticompensational stacking, is supported by numerous orbiter-based layer orientation measurements from sedimentary mounds on Mars including in and above the sulfate-bearing unit in Gale crater that show downslope layer attitudes (Kite et al., 2016). Characterization of the dips of VRR strata may inform which of these hypotheses is supported by the lowermost strata that compose Mount Sharp.

Here we analyze the orientation of 487 beds exposed along VRR using stereo Mastcam images taken at 24 sites to investigate the overall structure of the strata that make up VRR (section 4), place VRR in stratigraphic context with the rest of the Mount Sharp group, and investigate the origins of the lower portions of Mount Sharp. We compare the results of stereo image-based attitude measurements with independent assessments of the larger-scale structural orientation of units by making stratigraphic correlations between VRR and the Glen Torridon region (section 4.1). Results are compared with orbiter-derived attitude measurements of VRR (section 5.2).

2. Geological Setting

During its approximately 7-year mission so far on the Martian surface, the Curiosity rover has ascended more than 400 m of the lower slopes of Aeolis Mons (informally known as Mount Sharp), a ~5-km-high mound of sedimentary rocks preserved in the center of Gale crater. Along this traverse, strata consisting of fluvial, deltaic, lacustrine, and eolian sediments have been documented (Banham et al., 2018; Edgar

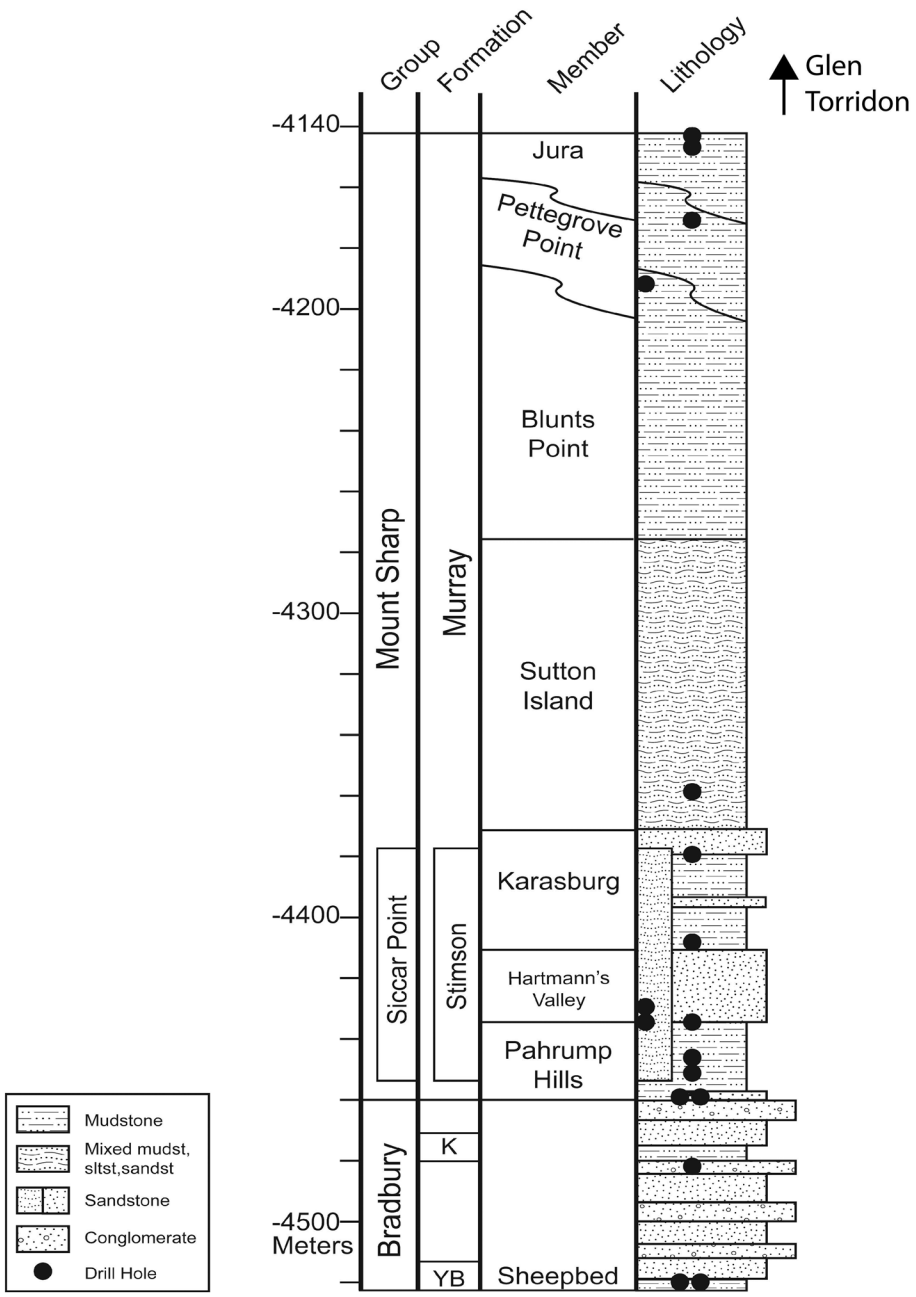

Figure 1. Stratigraphic column along Curiosity's traverse.

et al., 2017; Fraeman et al., 2016; Grotzinger et al., 2014, 2015; Minitti et al., 2019; Stack et al., 2019; Rivera-Hernandez et al., 2019, 2020; Williams et al., 2013) (Figure 1). These strata form three stratigraphic groups: (1) the Bradbury group, which sits at the base of Mount Sharp; (2) the Mount Sharp group, which interfingers with and overlies the Bradbury group; and (3) the Siccar Point group, which unconformably overlies the Mount Sharp group (Banham et al., 2018; Fraeman et al., 2016). The rover traverse through the Mount Sharp group has kept Curiosity within the Murray formation, a package of predominantly lacustrine mudstone with uncommon intercalated cross-stratified sandstones of prodeltaic, fluvial, or eolian origin (Edgar et al., 2017; Fedo et al., 2018; Grotzinger et al., 2015; Gwizd et al., 2019; Hurowitz et al., 2017; Rivera-Hernandez et al., 2020; Siebach et al., 2019; Stack et al., 2019). The Murray formation, which is at least 300 m thick, has been divided into seven members, the (presently) uppermost three of

which are measured in this study. These seven members include, in ascending order, the Pahrump Hills member, Hartmann's Valley member, Karasburg member, Sutton Island member, Blunts Point member, Pettegrove Point member, and Jura member (Figure 1). The Pahrump Hills member is dominated by thinly laminated mudstone interpreted to be deposited by hyperpycnal plumes in a freshwater lake (Grotzinger et al., 2015; Stack et al., 2019). The Hartmann's Valley member is characterized by decimeter- to meter-scale cross-stratified deposits indicative of eolian or fluvial reworking (Fedo et al., 2018; Gwizd et al., 2019). The Sutton Island member is a heterolithic mudstone-sandstone that largely consists of broken-up meter-scale blocks and contains textural evidence of periodic dry conditions in the form of desiccation cracks and sulfate enrichments (Rapin et al., 2019; Stein et al., 2018).

The strata measured in this study are limited to three members: the Blunt's Point member (BPm), the Pettegrove Point member (PPm), and the Jura member (Jm), due to their superior exposure relative to other members. The BPm consists of finely laminated mudstone interpreted to result from low-energy deposition of suspended mud in a lacustrine environment (Fedo et al., 2018; Bennett et al., this issue; Edgar et al., 2020; Rivera-Hernandez et al., 2020). Strata of the PPm and Jm form VRR, a ~200-m-wide, ~6.5-km long erosion-resistant topographic rise on the northwest flank of Mount Sharp (Fraeman et al., 2013, 2016; this issue). Although VRR is topographically distinct from surrounding strata, the Jm, PPm, and BPm are all dominated by finely laminated mudstones and thus assigned to the Murray formation. While the BPm-PPm and PPm-Jm contacts occur with well-exposed outcrops and clear topographic expressions, they do not follow elevation contours (Edgar et al., 2020). The same is true for the SIm-BPm contact, which lies far below VRR. Present understanding of these contact trends is most consistent with postdepositional deformation (C. Fedo et al., personal communication, September 2019) or lateral facies variations (Edgar et al., 2020).

Additional regional geologic context is provided by considering the relationship between strata that comprise VRR and surrounding units. Since leaving VRR, Curiosity began to explore Glen Torridon, a region directly south of VRR characterized by detection of smectite clay minerals in data from the Compact Reconnaissance Imaging Spectrometer for Mars (Fox et al., 2019). The northern part of Glen Torridon, traversed by Curiosity through Sol 2439, is composed of laminated mudstones with uncommon cross-bedded sandstones shaped into smooth, northeast trending ridges (Bennett et al., 2019, 2020) interpreted as periodic bedrock ridges (Stack et al., 2019). At least a portion of northern Glen Torridon, which is topographically lower than parts of VRR, is likely stratigraphically equivalent to the Jm (this paper). Orbital data show the clay-bearing strata of Glen Torridon are overlain by hydrated sulfate-bearing strata that may represent a transition to drier environments in Gale crater (Grotzinger & Milliken, 2012; Grotzinger et al., 2015; Fraeman et al., 2016; Fox et al., 2019; Milliken et al., 2010), and these strata are referred to as the sulfate-bearing or fractured-intermediate unit in this paper.

3. Methods

3.1. Plane Fitting Using PCA

3.1.1. Point Extraction

The Curiosity rover collects stereo images from two sets of cameras: Navigation cameras (Navcams) and Mast Cameras (Mastcams). The Mastcams consist of two cameras with different focal lengths and a stereo baseline of ~24.5 cm (Bell et al., 2017; Malin et al., 2017). The left Mastcam has a focal length of ~34 mm and collects images at up to 450 μm/pixel from 2 m, and the right Mastcam has a focal length of ~100 mm and collects images at up to 150 μm/pixel from 2 m (Bell et al., 2017; Malin et al., 2017). Each Navcam camera pair is separated by a 42.4-cm stereo baseline, thus offering ~2.15 times better stereo range error than Mastcams (Maki et al., 2012) but ~3.73 times lower spatial resolution. Mastcam and Navcam stereo images can be used to digitally trace bedding planes for orientation measurements. This study focuses on stereo Mastcam images because their color and higher angular resolution generally yield more accurate traces than Navcam images. Attitudes calculated from Mastcam-based traces were validated against Navcam-based traces in some instances. For each stereo Mastcam pair, coregistered rasters of (x,y,z) points and (x,y,z) errors were generated using Jet Propulsion Laboratory's Multimission Image Processing Lab stereo pipeline (Abarca et al., 2019; Alexander & Deen, 2017).

Bedding traces are digitized from RGB images, typically using higher resolution right Mastcam images, and the elevations and errors of their constituent points are generated from coregistered elevation models. The

(x,y,z) points are defined in site frame, a Mars-fixed rover operations coordinate frame in which $+x$ is defined as north, $+y$ as east, and $+z$ as gravity nadir (down). The result is an array of three-dimensional points that collectively represent a bedding plane and a second array that represents the stereo range error of each point along the trace projected into Cartesian space.

3.1.2. Finding the Nominal Plane

Previously, rover-based assessments of bedding orientations were performed visually (e.g., Arvidson et al., 2011; Grotzinger et al., 2015) or calculated via ordinary least squares (OLS) regression (e.g., Lewis, Aharonson, Grozinger, Squyres, et al., 2008; Lewis & Turner, 2019) or principal component analysis (PCA) regression (e.g., Hayes et al., 2011). OLS regression, in which planar geologic surfaces are modeled by fitting sets of coordinates to a best fitting plane, is perhaps the most popular technique for quantifying attitudes in remotely sensed data. A drawback of OLS regression is that it effectively imparts all errors to a dependent variable, typically the vertical plane, which may be unreasonable if errors are not chiefly vertical (Quinn & Ehlmann, 2019b). Our study utilizes a PCA regression method developed by Quinn and Ehlmann (2019b), which simultaneously fits errors along all axes, making it especially relevant when errors are nonvertical, which is known to be the case for stereo Mastcam images in which primary errors are along the range axis (see section 3.1.1).

In this section, we detail fundamental aspects of the PCA model as it pertains to this work. More information about the model and its derivation can be found in Quinn and Ehlmann (2019b).

PCA converts observations of putatively correlated variables into sets of linearly uncorrelated variables, or principal components. PCA is commonly used for dimensionality reduction, for example, for identifying or reducing the set of explanatory variables. When fitting the orientation of planes, however, PCA simply rotates orthonormal spatial coordinates (x,y,z) into a frame aligned with the planar fit ($\bar{x}_1$, $\bar{x}_2$, $\bar{x}_3$). Hence, the method does not entail any dimensionality reduction (Quinn & Ehlmann, 2019b).

The application of PCA for bedding plane fits starts with a digitized bedding trace, which yields an $n \times 3$ data matrix $\mathbf{D}$ containing the three-axis coordinates of points along the trace in site frame (e.g., Figures 3 and 7). The number of independent observations, n, that comprise the bedding trace typically ranges from several dozen to hundreds of points in Mastcam images. $\mathbf{D}$ is centered by subtracting the mean along each axis, $\boldsymbol{\mu}_\mathbf{D}$, as

$$\mathbf{M} = \mathbf{D} - \boldsymbol{\mu}_\mathbf{D}, \tag{1}$$

yielding the mean-corrected $n \times 3$ data matrix $\mathbf{M}$. Fundamentally, the PCA can be computed by performing an eigenvector decomposition of the sample covariance matrix. Quinn and Ehlmann (2019b) implement the PCA using singular value decomposition to produce an orthonormal coordinate basis $\bar{x}$, which is aligned with the directions of greatest variability within the data. $\bar{x}_1$ and $\bar{x}_2$ are within the best fitting plane through the data, while $\bar{x}_3$ is normal to the plane, and scatter along $\bar{x}_3$ represents error in the plane fit. The equation of the nominal plane is

$$n\,x + x \cdot \boldsymbol{\mu}_\mathbf{D} = 0, \tag{2}$$

where n is the normal vector of the nominal plane, defined as $n = v_3$ (the third eigenvector row of V) and x is the set of points within the nominal plane. The strike and dip of the nominal plane are then calculated as

$$(\text{strike}, \text{dip}) = \left(\tan^{-1}\frac{n_1}{n_2} - \frac{\pi}{2}, \cos^{-1}\frac{n_3}{\|n\|}\right). \tag{3}$$

This PCA framework immediately provides a means of assessing quality of fit. $\bar{x}_1$ and $\bar{x}_2$ define the extent of the plane to be fit. If $\bar{x}_2 \ll \bar{x}_1$, the fit is for a line rather than a plane, and such cases should be excluded. In contrast, planes with sufficient extent in $\bar{x}_1$ and $\bar{x}_2$ are well fit with errors lying in $\bar{x}_3$ (see also section 3.1.4).

3.2. Error Quantification

3.2.1. Error Sources and Representation

To fully contextualize structural measurements considering often unpredictable errors and variable terrain, we adopt the PCA-based error approach of Quinn and Ehlmann (2019b), which provides a method that

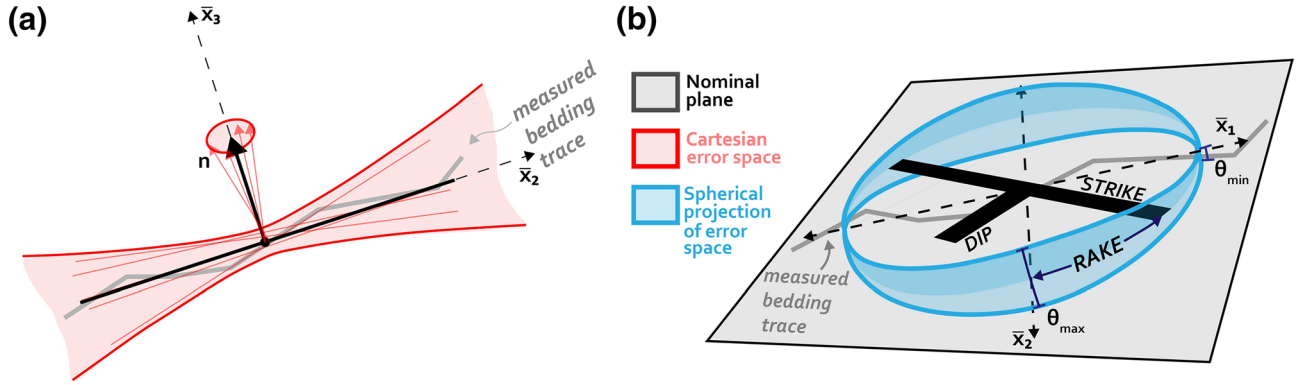

Figure 2. (a) Schematic representation of an $\bar{x}_2$-$\bar{x}_3$ slice of the nominal plane fit and errors in the Cartesian coordinate system. **n** is the normal vector of the nominal plane, which falls along $\bar{x}_3$. The shaded red region denotes the hyperbolic error space comprised of plane fits with different orientations. (b) Schematic representation of the error space to the plane (denoted by θ_{min} and θ_{max}) and rake angle in spherical coordinates. After figure from Quinn and Ehlmann (2019b).

simultaneously treats different error structures. A major advantage of PCA for plane fitting is that it accounts for errors along all axes simultaneously, which allows for fitting of planes that drape surfaces with varying error structures, including nonvertical errors (Quinn & Ehlmann, 2019b).

In performing geological orientation measurements with remotely sensed data, two predominant types of error arise: (1) measurement errors in bedding traces and (2) errors resulting from outcrop geometry or improper interpretation of bedding surfaces. Errors of the second type are discussed further in section 3.3. There are several sources of measurement errors, chiefly error in the construction of the photogrammetric DEM resulting from image misregistration, an especially difficult problem for Mastcam stereo images because the cameras have different focal lengths. Other major sources of measurement error include resampling error, sampling error due to inexact digitization of measured features, and downslope bias.

In Cartesian space, orientation errors in regression of a best fit plane can be represented by two hyperboloids that bound the set of all possible planes fitting the data set, which vary around the nominal regression solution, or as a set of normal vectors perpendicular to each plane solution (Figure 2a). Regression errors can be readily mapped from Cartesian to spherical coordinates. In spherical coordinates, orientations are frequently represented as pairs of angles (e.g., strike and dip or dip and dip direction). Errors are sometimes also parameterized in terms of strike and dip (e.g., Lewis & Aharonson, 2006), although orientation errors are not necessarily aligned with strike and dip and may be especially inaccurate in the case of near-horizontal bedding (Quinn & Ehlmann, 2019b).

After being mapped to spherical coordinates, the hyperbolic errors to the nominal plane defined in Cartesian coordinates define a spherical girdle of errors. In the convention of Quinn and Ehlmann (2019b), the span of this girdle is described by θ_{max}, the maximum angular error to the plane, and θ_{min}. θ_{max} is not necessarily parallel to the strike or dip. Instead, the orientation of θ_{max} with respect to the nominal plane solution is described by the rake angle between θ_{max} and the strike of the nominal plane (Figure 2b). In this study, errors are reported using this spherical framework because it allows for their conceptually straightforward visualization.

3.2.2. Error Quantification and Representation

Regression errors are modeled using a "variance-limited" framework in which the orientation of the PCA regression is equivalent to the PCA eigenvalues, that is, $\left[\frac{\lambda_3}{\lambda_1}\ \frac{\lambda_3}{\lambda_2}\right]$. In the variance-limited framework, the variance of the input data set provides a lower bound on errors to the nominal plane; plane fits to data sets with high variance yield high errors regardless of data density (Quinn & Ehlmann, 2019b). Because the precision of the mean of the data set is modeled by its variance, which is inversely proportional to $n-1$, small angular errors might be reported in mean-limited cases for data sets with large sample sizes despite inherently high variance (Quinn & Ehlmann, 2019b). Hence, the adoption of a variance-limited framework allows comparison of planes with different sampling statistics and sanctions the adoption of a Monte Carlo approach for the incorporation of stereo Mastcam errors (section 3.2.3) without skewing error statistics.

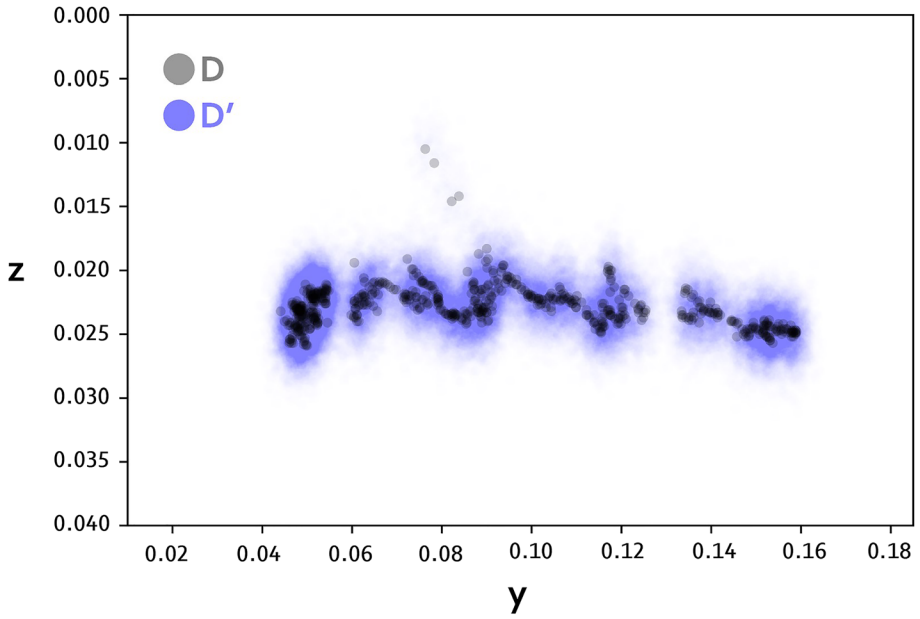

Figure 3. An example of all (x,y,z) points (**D**, in black) along a single bedding trace in the y-z plane and the set of points generated from stereo errors (**D′**, in blue). The blue points represent the data set that is fed to the PCA model. The average magnitude of y errors in this scene is approximately four times that of the z errors.

3.2.3. Incorporation of Axially Asymmetric Stereo Errors

Errors for photogrammetric data sets typically depend on the viewing geometry of the input images; oblique (near parallel to terrain) images predominantly produce errors in the line of sight. For MSL, these errors are typically expressed in the x and y axes in site frame, which frequently have errors more than an order of magnitude higher than those along the gravity nadir (z) axis. In these cases, if the input data matrix **D** from equation 1 contains only (x,y,z) coordinates from each bedding trace, the contribution of horizontal stereo errors would be systematically underestimated, which could lead to acceptance of solutions strongly biased by stereo errors along one axis. Instead, equation 1 is adjusted to ingest a modified input data matrix **D′**:

$$\mathbf{M} = \mathbf{D}^{'} - \boldsymbol{\mu}_{\mathbf{D}}, \tag{4}$$

where

$$\mathbf{D}^{'} = \begin{bmatrix} x_1 + \delta_{1x}{\sim}N[0x_{1e}] & y_1 + \delta_{1y}{\sim}N[0y_{1e}] & z_1 + \delta_{1z}{\sim}N[0z_{1e}] \\ \vdots & \vdots & \vdots \\ x_1 + \delta_{qx}{\sim}N[0x_{1e}] & y_1 + \delta_{qx}{\sim}N[0y_{1e}] & z_1 + \delta_{qx}{\sim}N[0z_{1e}] \\ \vdots & \vdots & \vdots \\ x_n + \delta_{qx}{\sim}N[0x_{ne}] & y_n + \delta_{qx}{\sim}N[0y_{ne}] & z_n + \delta_{qx}{\sim}N[0z_{ne}] \end{bmatrix}_{qn\times 3} \tag{5}$$

is a $qn \times 3$ matrix containing (x,y,z) points perturbed by normally distributed samples (δ_{qx}, δ_{qy}, δ_{qz}) of stereo errors (x_e,y_e,z_e) generated for each Mastcam image. q denotes the number of resampled points for each coordinate, and n, as before, is the number of independent measurements that comprise a bedding trace. (x_e,y_e, z_e) is the estimated stereo error along each site frame axis, calculated by projecting the range error (error in the downrange and cross-range directions from the camera) along the axes (Deen et al., 2019). The range error e is calculated as

$$e = \frac{r^2 ic}{b}, \tag{6}$$

where r is the range from the camera, i is the instantaneous field of view, c is the correlation accuracy, and b

is the stereo baseline. For each set of points (x_1,y_1,z_1) and their corresponding stereo errors (x_{1e},y_{1e},z_{1e}), q new sets of points are generated by adding the original coordinates to a sample of a normal distribution with a mean of 0 and a standard deviation sourced from (x_{1e},y_{1e},z_{1e}) (e.g., Figure 3). q must be sufficiently large for $\mathbf{D'}$ to plausibly contain the true (x,y,z) locations of each point in a bedding trace. q was set to 1,000 for this study, as increases beyond 1,000 showed no significant changes to the computed error. A major advantage of utilizing the variance-limited error framework is that the addition of resampled points to the input data matrix does not artificially reduce the maximum angular error, as would be the case in a mean-limited framework (Quinn & Ehlmann, 2019b), allowing stereo errors to be handled with a bootstrap Monte Carlo approach without adversely affecting the accuracy of reported errors.

The Monte Carlo approach to incorporating stereo errors also relies on assumptions about the underlying structure of Mastcam stereo errors, namely, that they are represented by a normal distribution with a standard deviation of (x_e,y_e,z_e). In this study, we generate $\mathbf{D'}$ using different standard deviations and report results for each case: (1) an aggressive approach, and upper bound on error, where (x_e,y_e,z_e) represents one standard deviation of the normally distributed sample $(\delta_{qx}, \delta_{qy}, \delta_{qz})$; (2 and 3) less aggressive approaches where (x_e,y_e,z_e) represents three or five standard deviations of the normally distributed sample $(\delta_{qx}, \delta_{qy}, \delta_{qz})$.

3.2.4. Impact of Stereo Errors on Plane Fits

Perhaps the greatest challenge of rover-based dip measurements is that the spatial extent of outcrop traces is generally low relative to their stereo errors. Even for exceptional outcrops, the ratio of trace extent to error along the first and second principal component axes may be 1 to 2 orders of magnitude lower than in traces performed using High Resolution Imaging Science Experiment (HiRISE) images because beds visible in HiRISE images can frequently be traced for hundreds of meters. Hence, stereo errors may comprise a significant fraction of the variance along bedding traces. Any trace with a high ratio of error to trace extent (δ_d/d) along a given axis is subject to two effects: (1) the solution space of the plane fit will trend toward an axis orthogonal to the direction with the greatest error and within the plane as (δ_d/d) increases; (2) the average dip of the solution space of the plane fit will decrease as (δ_d/d) increases. These effects are demonstrated in Figure 4, where a set of three points defining a plane dipping 5° toward 315° (NW) is perturbed by ever-increasing errors along the x (Figure 4b) and y (Figure 4c) axes using the approach of section 3.2.3 and the corresponding solution space is shown for each case. Similar effects can be seen in Mastcam-derived attitudes for small or distant traces (see section 4.1.1).

3.2.5. Joint Fitting of Parallel Bedding Planes

Even on VRR, which has some of the largest continuous outcrop exposures in the Murray formation, the lack of continuous exposures and/or bedding planes exposed in multiple dimensions is a common problem. As a result, many individual bed traces in Mastcam stereo images barely exceed stereo errors along one or more trace axes. However, in many scenes, closely spatially associated beds cut topography in different directions, yielding traces with varying coverage and orientation error structures. Hence, although the three-dimensional definition of all individual bedding traces within a scene may yield poor fits, the traces in aggregate may contain enough spatial definition for a high-quality planar fit. Under the assumption that bedding is parallel, based on visual observation of the measured beds, multiple traces are combined and fit jointly. The input data matrix $\mathbf{D'}$ for each bedding trace is centered on its mean and stacked with other mean-centered matrices to form a combined matrix that contains orientation information for each bedding trace independent of their relative locations. This combined data matrix is regressed using the same PCA technique (Quinn & Ehlmann, 2019b). Results of jointly fit bedding planes are shown for each scene in this study in addition to individual plane fits.

3.3. Outcrop Selection

This study uses Mastcam stereo pairs collected at 24 different sites across VRR between Sols 1802 and 2259 (Figure 5). Of these, five are in the Blunts Point member (BPm), three are in the Pettegrove Point member (PPm), nine are in the Jura member (Jm), four are on the BPm-PPm contact, and three are on the PPm-Jm contact. The distance to the measured outcrops ranged from ~2–20 m, and no outcrops were excluded from measurement based on range alone. Instead, specific measurements were dismissed based on the ratio of trace to error extent (sections 3.2.4 and 4.1.1), a metric implicitly related to outcrop range. The number of traces performed at each site is not constant; sites with greater exposure generally have more measurements. In total, 487 beds were traced with an average trace length of 14 cm and a median of 83

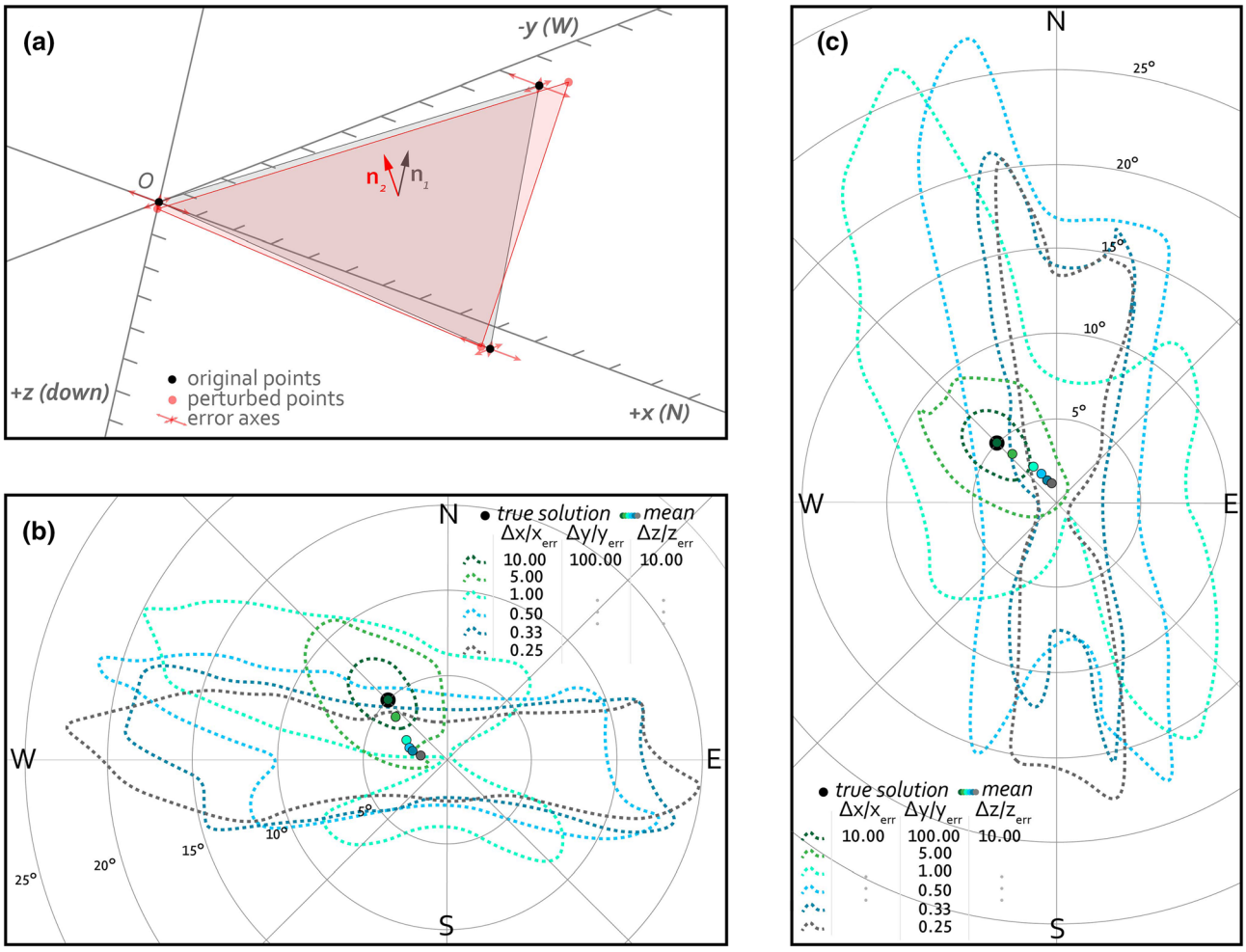

Figure 4. Example showing impact of stereo errors on solution uncertainty. (a) Schematic showing three points (black) in site frame that define a plane dipping 5° NW (the true solution in panels b and c), their axial errors (red arrows), and a set of perturbed points that defines a new solution. The axes are defined according to site frame. (b) Six different solution sets where the ratio of the extent of the bedding trace in the x direction to x errors (x/x_{err}) changes and y/y_{err} and z/z_{err} are constant. Dots denote the average solution. Dashed lines denote the range of possible solutions. Solutions are generated using the PCA-based Monte Carlo bootstrapping approach of section 3 where x_{err}, y_{err}, and z_{err} represent 1σ of the error. (c) Six different solution sets where (y/y_{err}) changes and x/x_{err} and z/z_{err} are constant.

points per bed prior to Monte Carlo repopulation (section 3.2.3). Stacked bedding traces were also performed at every site where multiple parallel beds could be measured.

Errors resulting from improper interpretation of bedding surfaces are a significant source of uncertainty in remotely sensed bedding orientation measurements. Poorly expressed bedding surfaces may not accurately capture primary depositional orientations for multiple reasons including: (1) rotation, faulting, or other forms of deformation and (2) traces of weathered surfaces, fractures, and/or diagenetic features that resemble but differ from primary bedding. To limit these sources of uncertainty, most measurements were performed on relatively large, intact outcrops (e.g., Figure 6a) that were less likely than individual blocks to have rotated during weathering but which may still have experienced regional postdepositional deformation that could result from multiple processes including impact cratering and differential compaction (Grotzinger et al., 2015). Most of these exposures are relatively oblique (e.g., Figures 6a and 7a), except along contacts (e.g., Figure 6c). Traces at seven of the sites were performed on blocks (Figure 6d) that may have rotated since deposition, although rotation was not obvious at any of the selected sites based on visual inspection alone. Beds that were obviously affected by localized deformation, such as near small impact craters on the ridge, were excluded. A potential error source especially prevalent on VRR is the accidental inclusion of low-angle crosscutting veins, which occur in the geomorphic transition to the ridge (Edgar

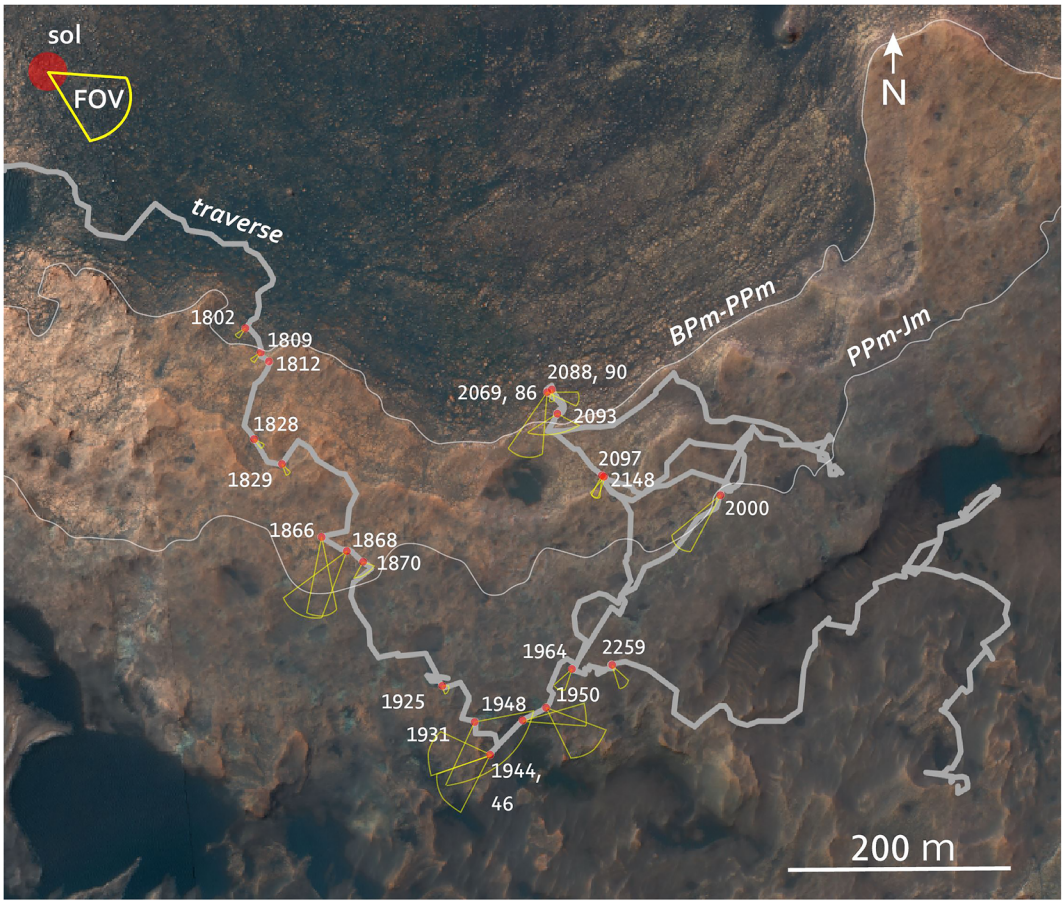

Figure 5. HiRISE overview showing sites with stereo Mastcams used in this study, labeled by sol. Yellow arcs denote the approximate field of view (FOV) of each image pair. The Blunts Point member-Pettegrove Point member (BPm-PPm) and Pettegrove Point member-Jura member (PPm-Jm) contacts are traced in white. The rover traverse is shown in gray.

et al., 2020; Fedo et al., 2018) and are locally difficult to distinguish from primary bedding where it becomes concordant (Figure 6b). All crosscutting features were excluded from analysis in this study. Beds were traced over the longest visibly contiguous span not affected by fractures or other crosscutting features. An example of a typical intact outcrop in the Jura member, associated bedding traces, and their plane solutions is shown in Figure 7.

4. Results

4.1. Bedding Orientation Results

4.1.1. Aggregate Orientation Results for Individual Bedding Planes

The dip and dip direction of all 487 individual beds are shown in Figure 8 for the 3σ stereo error case (section 3.2.3). Because uncertainties of individual bedding planes are often large, and because the distribution of sites and the number of traces performed at each site is nonuniform, the aggregate of individual solutions reported in Figures 8 and 9 should not be interpreted to necessarily correspond to a bulk regional orientation. In aggregate, the average orientation of individual plane fits is highly variable and generally dips between 0° and 10°. The average dip of all individual beds in the 3σ and 1σ stereo cases is shown in Figures S1 and S2 in the supporting information. In the 1σ stereo case, the average dip clusters along E-W and N-S axes and around 0° dips, symptomatic of the effects of large, axially asymmetric stereo errors discussed in section 3.2.3. Indeed, these solutions generally correspond to traces with low extent to error ratios (white points). In the 3σ case (Figures 8a and S1), attitudes do not cluster as strongly along E-W and N-S axes because stereo errors comprise a smaller fraction of the variance along $\overline{x}_3$. The uncertainties associated with

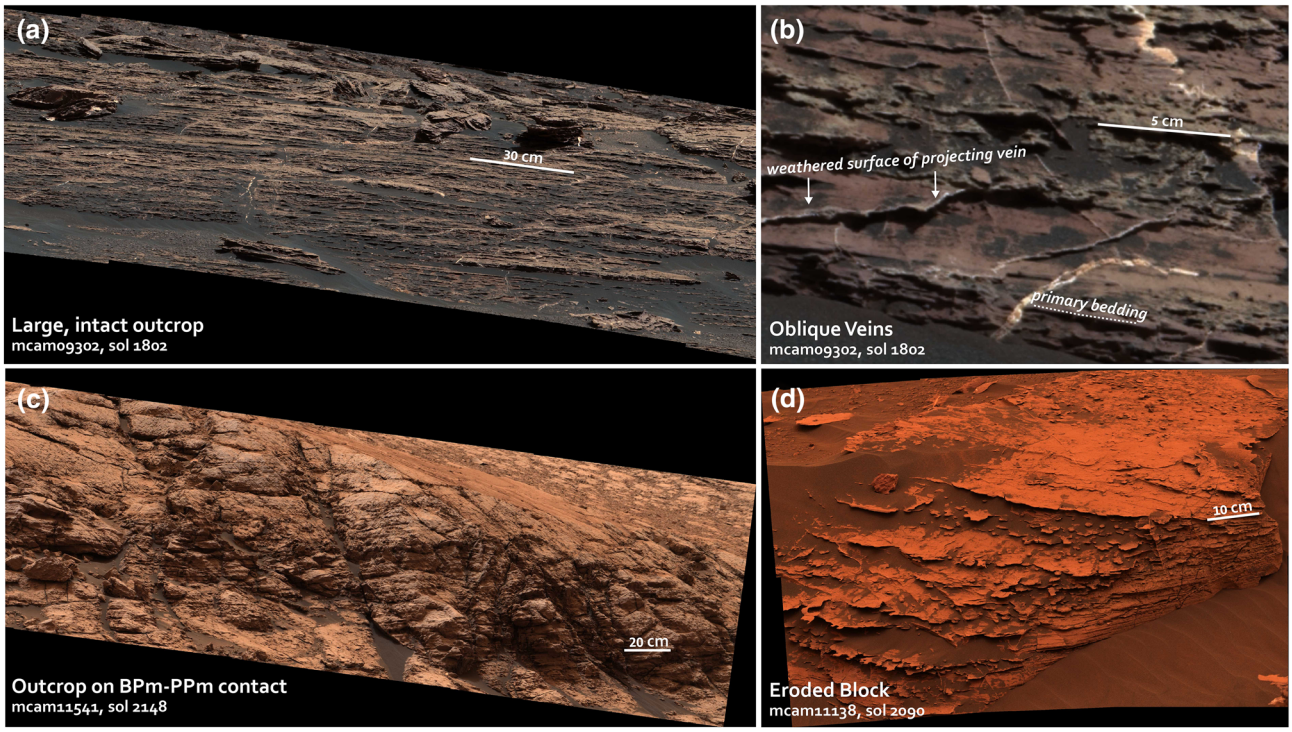

Figure 6. Examples of common outcrop geometries with traceable bedding on VRR. (a) A large, intact outcrop encountered on Sol 1802. (b) A portion of the same image showing low-angle weathered surfaces oblique to primary lamination. (c) A large, intact outcrop on the BPm-PPm contact imaged on Sol 2148. (d) A large, possibly rotated block with fine, parallel lamination imaged on Sol 2090.

the 1σ stereo error case are unrealistically high, and therefore, the 3σ stereo error case is likely more physically realistic. Traces whose spatial extent did not exceed the error by at least a factor of three along $\bar{x}_1$ or $\bar{x}_2$ were removed from subsequent analysis. The factor of 3 was chosen to capture solutions clearly dominated by stereo errors without removing a significant number of "good" fits, although all accepted solutions are skewed at least somewhat by stereo errors.

Figure 8b, again presented without uncertainties, shows the broad classification scheme corresponding to each plane fit for accepted solutions from Figure 8a: (1) large, intact outcrops (e.g., Figures 6a, 6b, and 7a); (2) large, intact outcrops that are also on member contacts; (3) individual blocks that may be more subject to rotation during weathering; (4) large, intact outcrops on slopes exceeding 20°, which may also be on member contacts. These categories were selected because they may be subject to different amounts of post-depositional deformation or modification and because they show systematically distinct orientation solutions. Most beds that dip to the north are found on the BPm-PPm or PPm-Jm contacts, which themselves dip north as mapped by HiRISE (Tables 1 and 2), although dips measured on those contacts do not exclusively dip northward. Most beds with an average dip solution of more than 10–15° in any direction are on topographic slopes of at least 20°, which include but are not limited to member contacts in some areas, or in individual blocks. The average dip angle and azimuth of beds measured in intact outcrops not associated with member contacts is also variable, but mostly ranges from 0–10°SE. Although the uncertainty of most plane fits for individual beds is generally high, regional bedding attitudes can be constrained by consideration of the most exceptional outcrops (section 4.1.2).

4.1.2. Site-Specific Orientation Results for Individual and Stacked Bedding Planes

Figure 9 shows the projection of errors to bedding poles for all measured beds accepted in section 4.1.1 using the 3σ stereo error case discussed in section 3.2.2. Corresponding plots for the 1σ and 5σ stereo error case are shown in supporting information Figures S3 and S4, respectively. Solutions corresponding to stacked traces, which represent either a subset or the full set of traces within a scene, are also shown in Figure 9, and the probability distribution of the dip magnitude of each stacked solution is shown in Figure 10. Although the dip azimuth of individual bed solutions is collectively high (Figure 8), dip azimuths typically cluster more

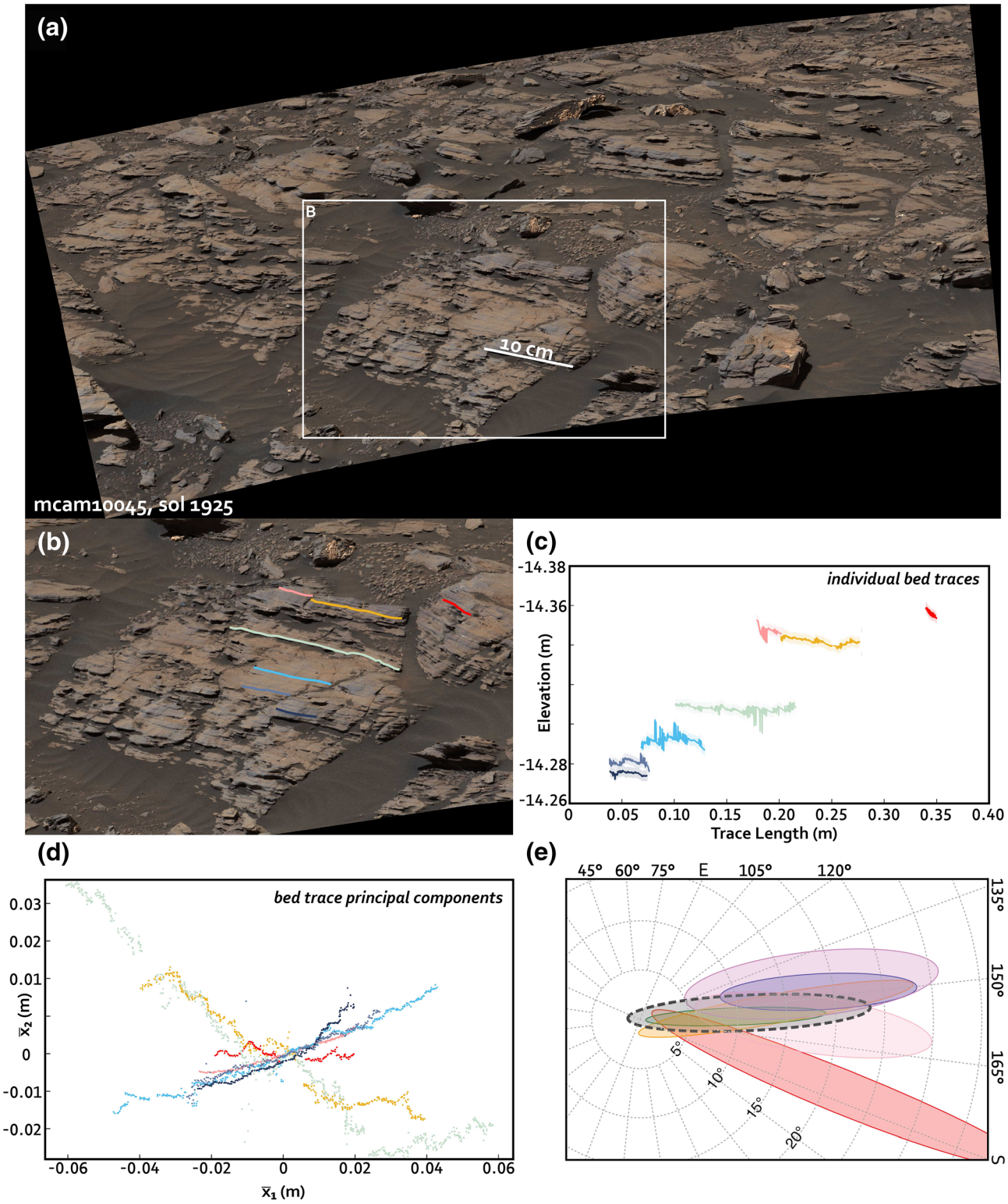

Figure 7. Representative example of bedding traces and resulting PCA plane fits. (a) Intact outcrop imaged in the Jura member on Sol 1925. (b) Enlarged portion of (a) with colored bedding traces. (c) Elevation (m) as a function of trace length, color coded by trace. (d) Each trace projected along its first and second principal components. (e) Azimuthal plot of uncertainties in dips and dip directions for each example trace.

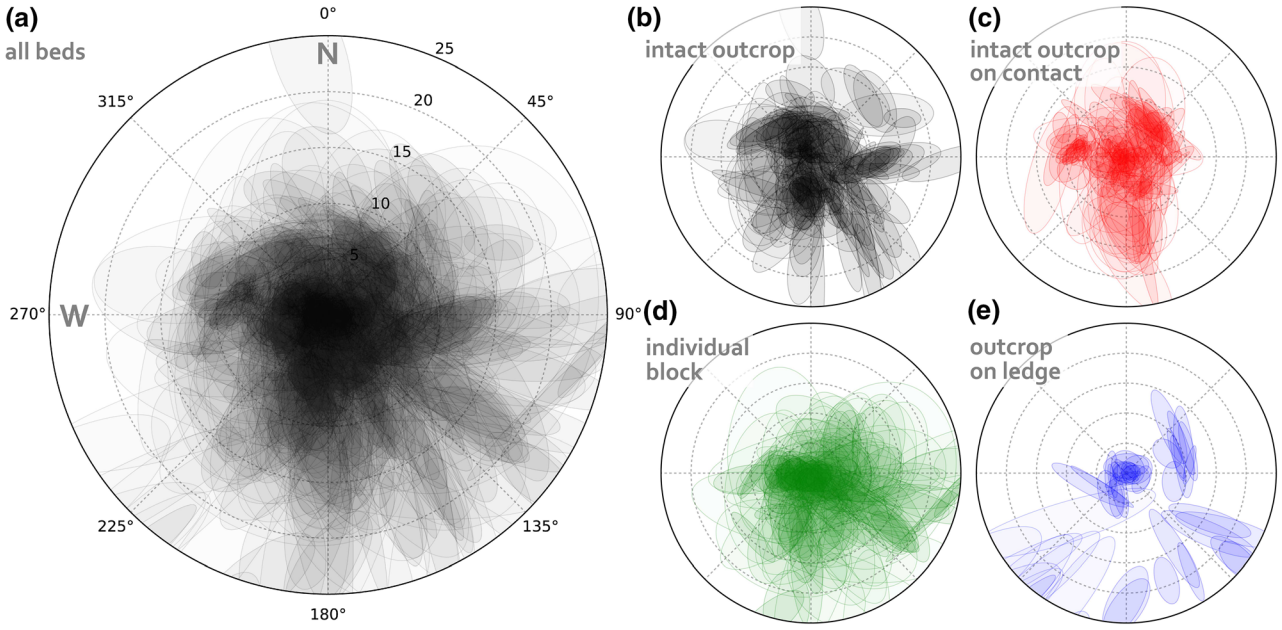

Figure 8. (a) Dip angle and dip direction of every bed measured in this study using the 3σ stereo error case. Each ellipse represents the range of possible solutions for one bedding plane. (b–e) Classification of the solutions from (a) according to whether the bed is part of an intact outcrop (b), an intact outcrop on a contact (c), an individual block (d), or an outcrop on the side of a ledge, defined here as a regional slope >20° (e).

tightly within individual scenes, consistent with the expectation that beds within a given scene should dip in similar directions if they are parallel-stratified lacustrine mudstone. It is also possible that bedding comprises topographic features such as mounds or depressions larger than the scale of outcrops observed by the rover but smaller than the scale over which orbit-based measurements are made, in which case the assumption of consistent dip azimuths within individual scenes remains valid. More credence should be lent to stacked solutions than individual solutions because they have larger trace extents in $\bar{x}_1$ and $\bar{x}_2$ and buffer against the inclusion of poor or otherwise unrepresentative traces. All stacked measurements are summarized in Table 1 for the 3σ stereo error case.

In 7 of the 24 scenes, even stacked bedding traces do not exceed the trace to error threshold of a factor of three (Table 1 and section 4.1.1) and should be regarded with skepticism because the dip magnitude and azimuth are likely more heavily influenced by stereo errors than in other scenes. Caution should be taken in comparing the average dip of each scene (Table 1) because the uncertainties of plane fits in some scenes is so large as to be effectively unconstrained, thus making it possible that the true attitude and average solution differ significantly. There is no clear correlation between the stacked dip azimuth and regional slope in a scene, which indicates that downslope bias is not a major contributor to the plane solutions.

The smallest stacked error ellipses, which represent the best constrained attitudes, occur in scenes from Sols 1809, 1829, 1866, 1944, 1946, 1950, 2000, 2086, and 2148. The Sol 1866 and 2000 mosaics record the PPm-Jm contact and reveal average dips of ~6.5° toward 32° and ~7.8° toward 285°, respectively, which are close to the dip of the entire contact (6.56° toward 332.1°), though other, worse constrained measurements (Sol 1868) on the PPm-Jm contact dip S. The Sol 1809 and 2148 mosaics record the BPm-PPm contact and have median dips of ~3.5° toward 215° and ~1.8° toward 280°, respectively, which differ from the dip of the entire contact (7.30° toward 334.4°). The Sol 2086 scene sits in the BPm and has a median dip of ~1.8° toward 279.8°. The median dip solutions of other scenes in the BPm range from ~3°S to ~6°NW but have significantly larger error ellipses that encompass many solutions within that range. The Sol 1829 scene sits in the PPm and has a median dip of ~3.4° toward 262°, although the stacked traces were performed on a block and other beds in the PPm show a wide range of dips (e.g., Sol 1828, Table 1). The Sol 1944, 1946, and 1950 scenes are in the Jm and have median dips of ~0.6° toward 320.2°, ~5.1° toward 192.9°, and ~6.2° toward 219.7°. Several scenes in the Jm are likely proximal to small impact craters, but care was taken to exclude obviously deformed beds in these scenes. Other beds measured in the Jm dip predominantly ~0–15°S with larger error ellipses that encompass a wide range of solutions.

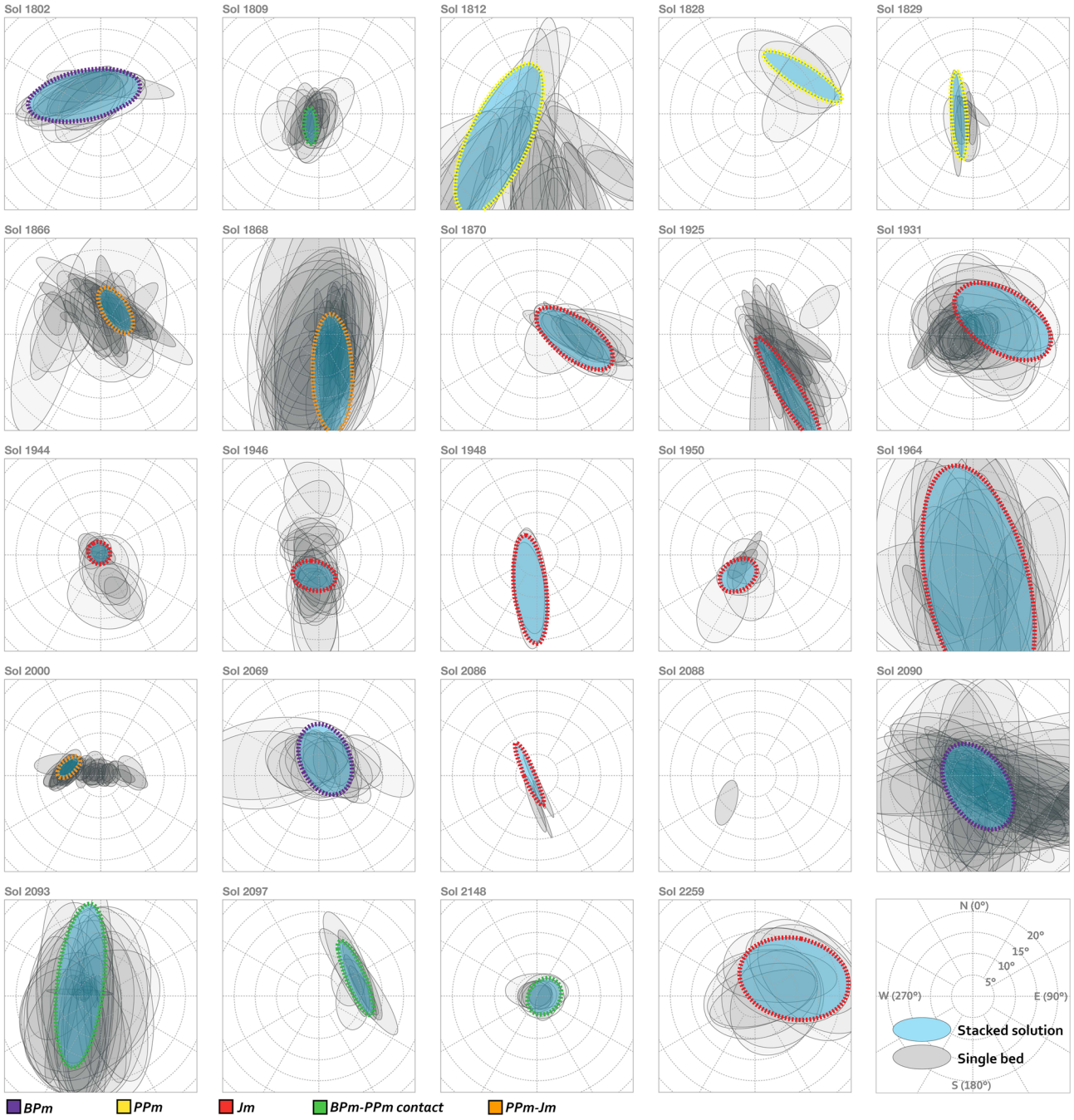

Figure 9. Range of possible dip and dip azimuth solutions at different sites, grouped by sol. Gray ellipses denote the solution space of individual bed traces. Blue ellipses denote the solution space of stacked traces from that sol (see Table 1). Not all individual traces shown were necessarily used to produce the stacked solutions for a given sol. All single bed solutions shown had trace extent to error extent ratios of at least five along the first and second principal component axes. Using 3σ error case.

4.2. Constraints on Bedding Orientation From Regional Geology

Due to the large uncertainties of plane fits for individual beds (Figures 9 and 10), changes in topography across the ridge, and asymmetric imaging and bed trace sampling, it is difficult to report a cumulative average dip direction and magnitude for the strata that comprise VRR based solely on individual plane traces with a confidence better than several degrees. It is possible, however, to validate rover-based bedding orientations and further constrain regional dips by analyzing the elevations where facies present on VRR reappear in the Glen Torridon trough, a much larger spatial scale of structural analysis.

Journal of Geophysical Research: Planets

10.1029/2019JE006298

Table 1
Dip Measurements of VRR Member Contacts From HiRISE and Stacked Dip Measurements From Stereo Mastcam Images on VRR (3Σ Stereo Error Case)

Sol or ID	Member	Outcrop type	Regional slope	Regional direction	dip *n*	Trace length (m)	Dip	Dip direction	θ_{min}	θ_{min}	Rake	$\mathbf{d}/\delta_{\mathbf{d}}$ second PC
Traces of VRR member contacts from HiRISE												
BPm-PPm contact	BPm-PPm	—	—	—	352	3,873	7.30°	334.4°	0.30°	3.74°	91.3°	—
PPm-Jm contact	PPm-Jm	—	—	—	140	1,076	6.56°	332.1°	0.22°	1.11°	71.7°	—
Joint fitting of parallel bedding planes on VRR												
1802	BPm	Intact	18.9°	32.0°	1,119	0.51	5.82°	317.9°	5.69°	13.34°	30.76°	3.86
1809	BPm-PPm	Intact	18.5°	7.6°	1,689	0.14	3.47°	214.6°	1.50°	4.28°	52.50°	4.98
1812	PPm (on ledge)	Intact	20.6°	353.9°	1,262	0.06	10.85°	236.4°	7.08°	19.39°	121.11°	14.30
1828	PPm	Intact	8.0°	316.0°	468	0.21	14.37°	52.1°	2.74°	10.60°	20.82°	6.76
1829	PPm (on ledge)	Blocks	36.3°	327.6°	827	0.13	3.40°	261.9°	1.79°	10.31°	175.83°	2.96
1866	PPm-Jm	Intact	18.7°	10.0°	1,781	0.25	6.64°	32.1°	2.97°	6.07°	25.22°	33.08
1868	PPm-Jm	Intact	12.4°	3.8°	320	0.20	9.75°	160.9°	4.67°	13.95°	107.69°	4.40
1870	Jm	Intact	15.3°	330.4°	808	0.11	8.96°	96.1°	4.77°	10.62°	60.85°	2.72
1925	Jm	Intact	14.3°	337.1°	1,615	0.13	15.57°	149.2°	2.57°	14.49°	89.57°	14.90
1931	Jm	Blocks	18.5°	351.6°	—	—	7.65°	66.7°	7.14°	12.65°	34.58°	3.68
1944	Jm	Intact	15.7°	79.6°	878	0.79	0.57°	320.2°	2.47°	2.72°	90.48°	4.21
1946	Jm	Intact	18.3°	92.8°	1,436	0.18	5.07°	192.9°	3.43°	5.09°	0.46°	2.95
1948	Jm	Blocks	12.8°	257.3°	348	0.84	8.33°	190.3°	3.76°	12.84°	73.35°	1.88
1950	Jm	Intact	17.9°	261.8°	527	0.47	6.24°	219.7°	3.46°	4.72°	73.89°	4.77
1964	Jm	Block	8.0°	346.2°	419	0.04	7.39°	170.6°	12.08°	29.01°	87.08°	2.71
2000	PPm-Jm	Intact	18.5°	355.8°	1,576	0.25	7.83°	284.5°	1.69°	3.26°	34.43°	10.51
2069	BPm	Intact	18.3°	340.9°	1,459	0.74	4.03°	22.4°	5.84°	8.60°	45.42°	3.19
2086	BPm	Intact	18.0°	336.1°	517	0.87	1.82°	279.8°	1.23°	7.90°	32.84°	16.90
2088	BPm	Block	19.7°	357.8°	—	—	—	—	—	—	—	—
2090	BPm	Block	—	—	1,190	0.06	2.89°	155.9°	7.06°	11.02°	81.78°	5.87
2093	BPm-PPm	Intact	18.0°	344.7°	614	0.36	5.40°	296.4°	5.44°	19.34°	20.04°	4.46
2097	BPm-PPm (on ledge)	Intact	24.1°	32.3°	659	0.46	9.72°	63.9°	2.21°	9.41°	3.42°	6.54
2148	BPm-PPm (on ledge)	Intact	48.0°	358.4°	502	0.13	1.76°	95.0°	3.67°	4.48°	154.80°	1.51
2259	Jm	Blocks	6.6°	54.4°	720	0.16	10.17°	66.2°	9.47°	13.02°	125.43°	2.04

Table 2
Orbiter-Based Attitude Measurements of VRR or Lower Gale Mount Sharp Strata

Study	Trace location	Dip	Dip direction	Comments
This study	BPm-PPm contact	7.30°	334.4°	—
This study	PPm-Jm contact	6.6°	332.1°	—
Milliken et al. (2010)	Lower member	1–6°	285–30°	Strata are above sulfate-bearing unit
Stack et al. (2013)	Lower member	7.9°	315°	Strata are above sulfate-bearing unit
Fraeman et al. (2013)	BPm	6.3–7.8°	~315°	—
Fraeman et al. (2013)	VRR	5.7–14.1°	~315–45°	—
Fraeman et al. (2013)	Glen Torridon	5.8–8.6°	~310–350°	—
Fraeman et al. (2013)	Sulfate-bearing unit	3.6°	345°	—
Kite et al. (2013)	Lower Gale mound	2.5–4.5°	~330°	Strata are below sulfate-bearing unit
Kite et al. (2016)	Lower Gale mound	3.1–4.2°	~330°	Strata are below sulfate-bearing unit

4.2.1. Dip of the Flodigarry Facies

On VRR, an ~5- to 7-m-thick laminated mudstone with distinct, alternating resistant (purple) and recessive (tan) beds defines the base of the Jura member of the Murray formation (Edgar et al., 2020). This characteristic "Flodigarry facies" sits at the PPm-Jm contact, which occurs at an elevation of −4,155 m at the easternmost part of the traverse (Sol 2013; Figures 11d and 11f). On Sol 2357, Curiosity encountered similar alternating resistant and recessive, tan- and purple-shaded beds at the target *Flodigarry* near one of the deepest parts of the Glen Torridon trough at an elevation of −4,152 m (Figure 11d). Due to its similar lithology to the rocks at the base of the Jura member of VRR, *Flodigarry* is interpreted to be part of the same stratigraphic interval (Edgar et al., 2020; Fedo et al., 2020). Using the elevations of the base of the Jura member and of the *Flodigarry* target, which collectively comprise an informally recognized Flodigarry facies, the regional bedding attitude of the Flodigarry facies can be evaluated. Notably, this estimate of bedding attitude is independent of both orbiter- and rover-based dips, which are based on local geometry.

Estimating the attitude of the Flodigarry facies requires knowledge of the elevations of the *Flodigarry* target and the PPm-Jm contact, the distance between them, and the position of the *Flodigarry* target within the stratigraphic interval. To account for different elevations along the PPm-Jm contact (Fedo et al., 2019), the dip of the Flodigarry facies was calculated using elevations sampled from a large portion of the contact (yellow line Figure 11d). To account for possible postdeposition deformation, the elevation of *Flodigarry* was perturbed by elevations equivalent to the magnitude of elevation variation measured along many 150-m segments of the PPm-Jm contact (the average distance between the PPm-Jm contact and *Flodigarry*) (black line, Figure 11e). Because the *Flodigarry* target is shallowly exposed, slopes were calculated under the assumption that the target occurs near the top of the facies and that the facies thickness varies minimally between 5 and 7 m as observed on VRR. Because the PPm-Jm contact defines the bottom of the facies on top of VRR, possible slopes of the Flodigarry facies can be estimated by tracing lines between points on the PPm-Jm contact and the elevation 5–7 m below *Flodigarry* (light gray line, Figure 11e), which fall between ~0°SE and 2°SE. The resulting range of possible dips of the Flodigarry facies is between ~4°SE and 2°NW, and 95% of solutions fall between 3.8°SE and 1.4°NW, consistent with an approximately flat stratal geometry extending through VRR and Glen Torridon.

4.2.2. Dip Constraints From the Projection of Contact Elevations

The strata that comprise VRR extend southward into the Glen Torridon trough where they are overlain by younger strata. This can be confirmed in situ due to the identification of the *Flodigarry* target in Glen Torridon and is also supported for the BPm, which is seen from HiRISE to extend several hundred meters into Glen Torridon west of the Greenheugh pediment where the positive topography of VRR tapers out (Figure S4). The extent of other VRR member lithologies in Glen Torridon may additionally constrain regional dips. The projections developed in section 4.2.1 can be extended to calculate the angle between the major member contacts and points throughout Glen Torridon. The BPm-PPm and PPm-Jm contacts on VRR were identified using a combination of ground-based and orbital mapping (Edgar et al., 2020) and traced in HiRISE images. For each point in a region of Glen Torridon, the angle between each point and the BPm-PPm and PPm-Jm contacts along an approximate NW striking (315°) dip angle was calculated (Figure 12).

In most portions of Glen Torridon, including along the rover traverse, the BPm would be exposed if it dipped more than ~5–7°NW (Figure 12b). East and west of the rover traverse, where the trough is slightly deeper,

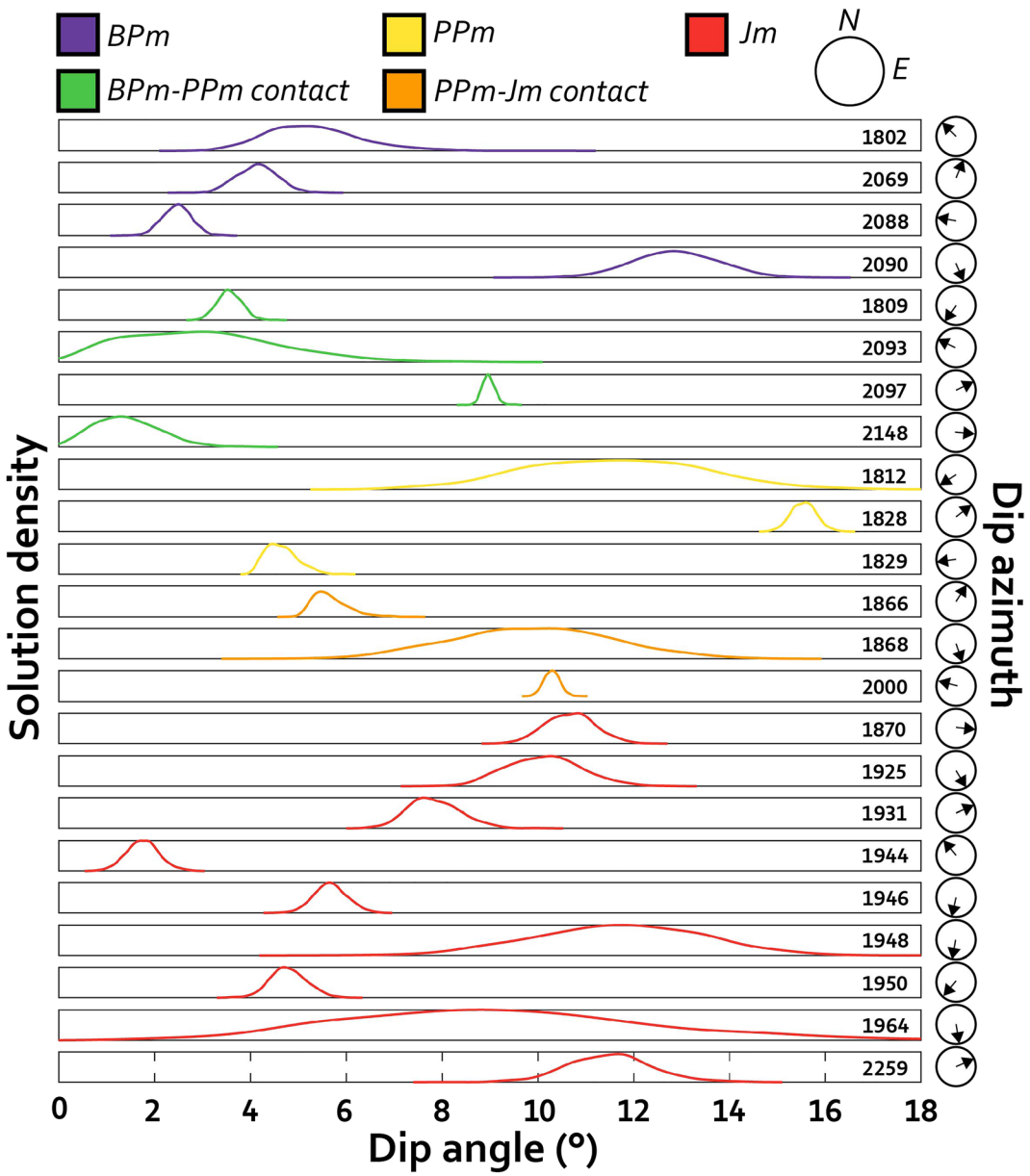

Figure 10. Probability density functions for each stacked solution displayed in Figure 9, grouped according to member. The average dip azimuth of each stacked solution is shown to the right. The ratio of trace to error extents is variable between solutions (see Table 1).

the required dips for exposure decrease to ~2.5–3°NW. The BPm, which is typified by mudstone characteristic of much of the Murray formation (Fedo et al., 2018), has not been identified in the area south of VRR along the rover's future traverse from either rover- or orbiter-based images, or east of the rover's location in deeper parts of the Glen Torridon trough. Assuming the BPm contiguously underlies the Glen Torridon strata, its absence from most mapped regions suggests the member can dip no more than ~2.5–3°NW. The magnitude of this constraint may vary slightly due to postdepositional deformation, and angle estimates grow increasingly uncertain farther from VRR, but values of <~2.5–3° are common throughout the mapped region. In most portions of the Glen Torridon trough, Jm strata would be exposed only if they dipped more than ~0–3.5°NW (Figure 12a). Although Curiosity has traversed this full range of angles, strata lithologically similar to the lower Jm have only been identified at one location—*Flodigarry*—which is located precisely where the angle between the PPm-Jm contact and Glen Torridon is the lowest (Figures 11a and 12a). Other strata along the first several hundred meters of the rover's traverse

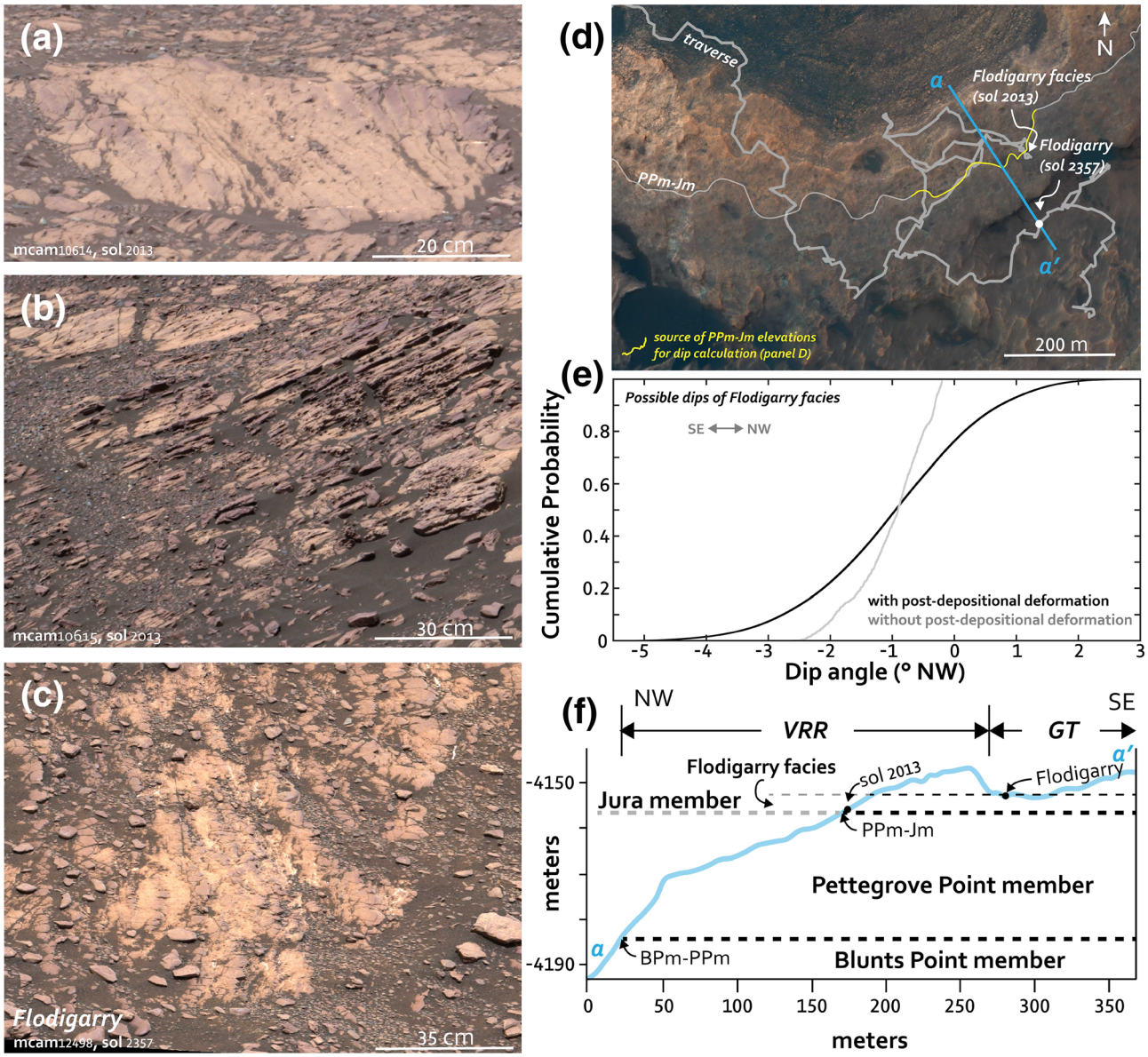

Figure 11. (a and b) Recessive tan- and purple-toned beds above the PPm-Jm contact (Sol 2013). (c) Recessive tan- and purple-toned beds of the Flodigarry target (Sol 2357). (d) a-a′ profile in (e) and location of images in (c) and (d). The portion of the PPm-Jm contact used to calculate dips of the Flodigarry facies is gold. (e) (gray line) Set of angles between the Flodigarry target and the gold portion of Jm-PPm contact using a Flodigarry target elevation offset by −5 m; (black line) same set of angles as the gray line, but allowing the Flodigarry facies to have deformed at scales similar to those observed on member contacts. (f) Transect across VRR and into the Glen Torridon trough showing the relative locations of the BPm-PPm and PPm-Jm contacts and the Flodigarry facies.

through Glen Torridon are interpreted as Jm, but do not share the same characteristics as the Flodigarry facies. If PPm or Jm dips are more than ~1–2°NW, Flodigarry strata should be identifiable across a several hundred-meter swath of the Glen Torridon trough. Collectively, results are consistent with regionally flat- or near-flat-lying stratal geometry for the Murray formation.

5. Discussion

5.1. Collective Interpretation of Dip Measurements

The uncertainty of most Mastcam-based plane fits is too large to yield a well-constrained dip and dip azimuth. The large uncertainties result primarily from the combination of poor bedding exposures (i.e., short extents in $\overline{x}_1$ and $\overline{x}_2$) and large stereo errors. In several scenes, however (section 4.1.2), the stacked plane

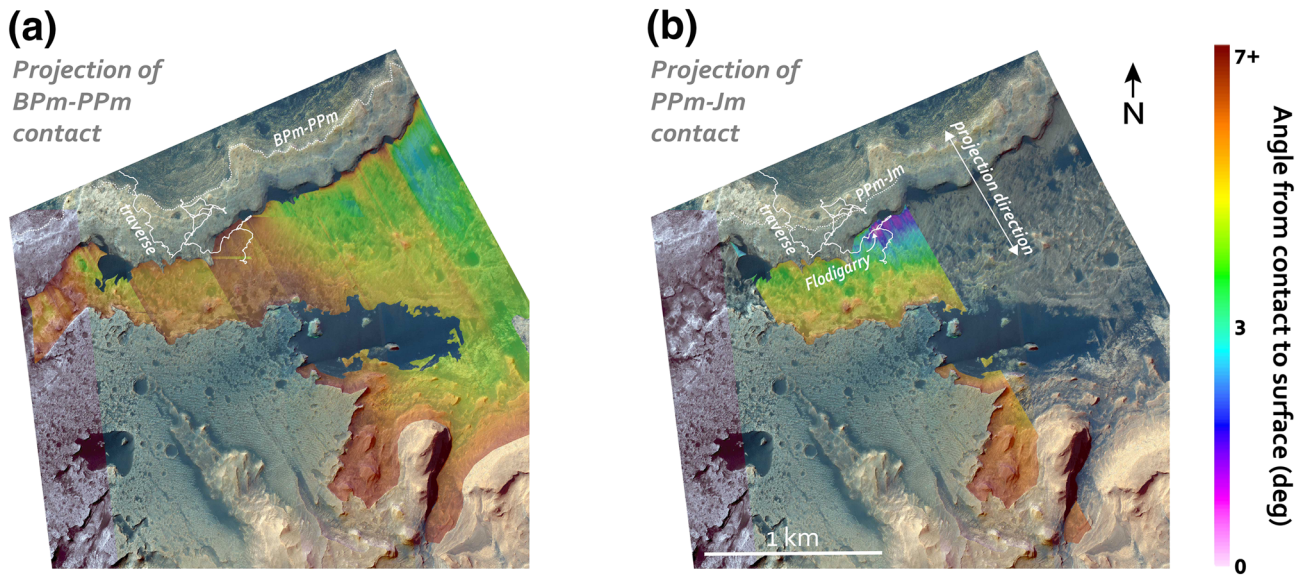

Figure 12. Map of the angle between the (a) PPm-Jm contact and surface and (b) BPm-Jm contact and surface projected along a line oriented toward 315° (arrows in a). The rover traverse is shown by the solid white lines. Angles are positive if they dip NW. The Flodigarry target is highlighted in (a).

fits are well constrained to a range of a few degrees of dip and ~15–60° of dip azimuth. Any attitude differences between these beds in excess of the reported uncertainties are likely real. Such outcrop-dependent attitude differences are common, and no single regional attitude is contained in the solution space of every stacked trace. For example, the stacked solutions from Sols 1829, 1866, and 1944 are relatively well constrained and do not overlap. The (up to 100°) different orientation of these beds is probably not primary due to their association with apparent secondary deformation processes but rather the result of weathering, gravity-driven motion or rotation of blocks, and localized postdepositional deformation that could result from multiple processes including impact cratering or differential compaction. Cross-beds deposited by some types of migrating bedforms could yield a wide range of primary dip azimuths including those in which the contacts bound an extreme of the field of observations (e.g., Rubin & Carter, 2006), although cross-beds were not positively identified on VRR (Edgar et al., 2020). In tandem with uncertainties stemming from the error structure of the traces, structural variation within VRR yields a murky picture of dips at a regional scale based on in situ bedding traces alone. Possible solutions for stacked dips in each member and member contact mostly range from ~2°N to 10°S in the Jura member, ~2–10°S in the Pettegrove Point member, ~6°SE to ~8°NW in the Blunts Point member, ~4–10°N on the BPm-PPm contact, and ~0–6° with variable azimuth on the PPm-Jm contact. The probability of solutions falling in this range is nonuniform, and most solutions sit near the middle of the range (Figure 10). That is, it is more likely that the true attitudes of most beds are closer to the middle of the uncertainty range than the extremities. Although the range of solutions is too variable collectively to confidently report an aggregate regional dip, they do not support regional dips greater than several degrees in any direction. There are beds on VRR that dip more than several degrees, but these solutions dip in multiple directions (Figures 9 and 10), are discrepant from most member orientations, and likely arise from either high stereo errors (e.g., Sol 2000), rotation (e.g., Sol 1870), or postdepositional deformation, probably mostly impact cratering (e.g., Sol 1944), which has a high retention rate at VRR.

Stratigraphic correlations between VRR member strata and Glen Torridon (section 4.1) further constrain the regional structural orientation. Correlation of the *Flodigarry* target with similar facies encountered by Curiosity in the lower Jm exposed on the northern flank of VRR constrain the dip of the Flodigarry facies to between ~3°SE and 2°NW (section 4.1.1). Projections of the BPm-PPm and PPm-Jm contacts SE indicate that Curiosity would have already encountered BPm strata in Glen Torridon if the dip were more than ~5° NW. Furthermore, BPm strata may be visible from orbit elsewhere in the Glen Torridon trough if the regional dip is more than ~2–3°NW, assuming lateral continuity (section 4.1.2). No BPm strata have been identified in Glen Torridon east of the Greenheugh Pediment, although it is possible that BPm strata are not

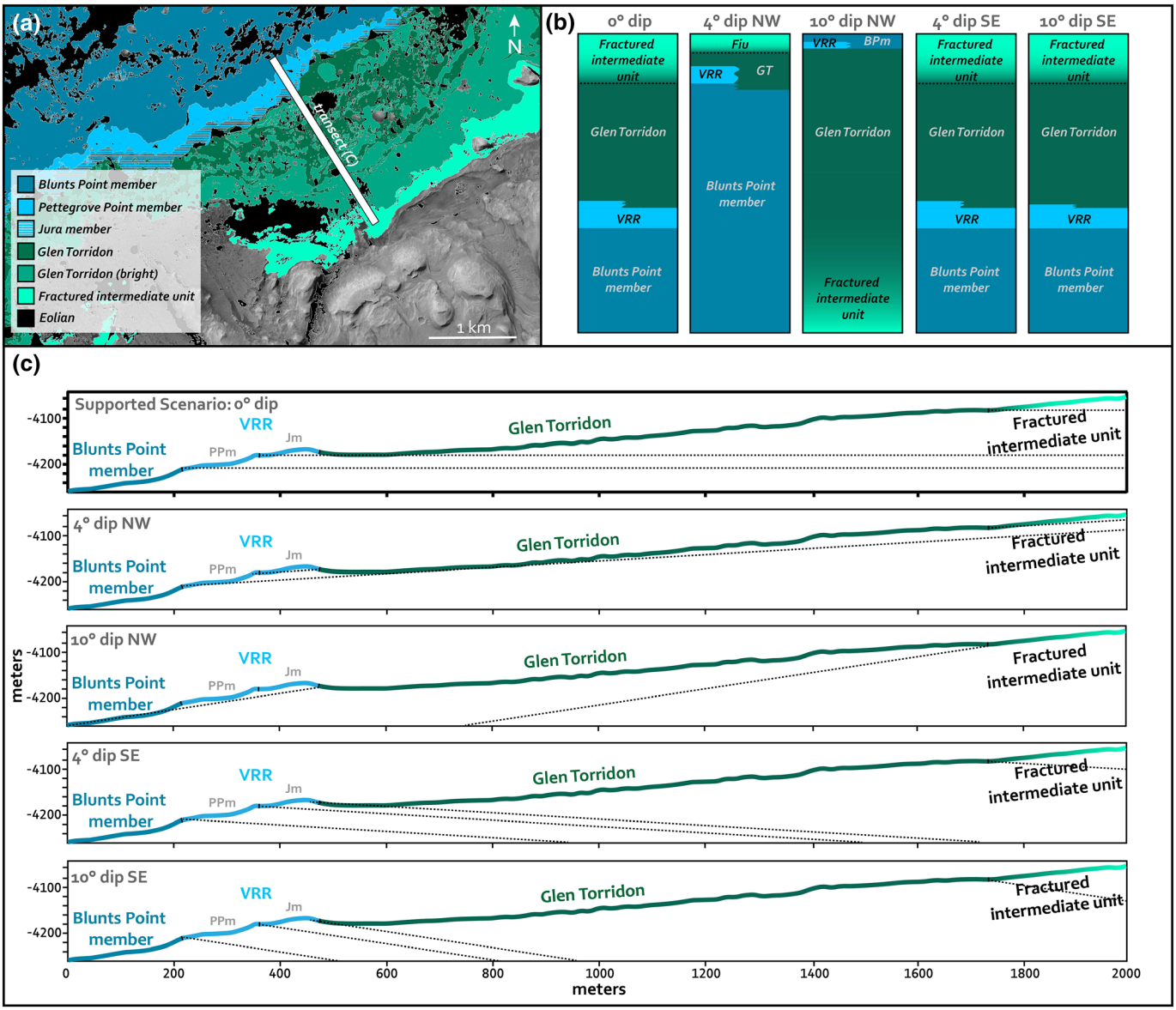

Figure 13. (a) Geological map showing the Blunts Point, Pettegrove Point, and Jura members, Glen Torridon, and the sulfate-bearing (fractured-intermediate) unit. Map adapted from Stack et al. (2017). (b) Notional stratigraphic columns for different regional dips along the white transect in (a). Unit thicknesses within the columns are approximately to scale. (c) Elevation profile along the white transect in (a). Dashed lines denote the projection of each unit under the surface following the regional dip cases in (b).

identifiable in HiRISE images. A similar exercise with the PPm-Jm contact indicates that Curiosity should have already encountered Jm strata if the regional dip is flat, which it did at *Flodigarry*. Collectively, regional stratigraphic correlations are consistent with dips between ~2°SE and 2°NW.

5.2. Comparison With Orbiter-Derived Dip Measurements

Previous studies have measured the attitude of features on VRR (Fraeman et al., 2013) and elsewhere on lower Mount Sharp (Kite et al., 2013, 2016; Milliken et al., 2010; Stack et al., 2013) using orbiter-based images and DEMs (Table 2). Orbiter-derived dips on Mount Sharp generally range from 2–8°NW. In the BPm and VRR, Fraeman et al. (2013) report dips of 6.3–7.8°NW and 5.7–14.1° predominantly NW, respectively. These are consistent with HiRISE-derived attitudes generated for the BPm-PPm and PPm-Jm contacts in this study (contacts shown in Figure 12), which dip 7.30° toward 334.4° and 6.6° toward 332.1°, respectively. Beds

measured along the PPm-Jm contact in Mastcam images mostly dip shallowly S or WNW, unlike the HiRISE-based contact (section 4.2 and Table 1).

Although orbiter-based dip measurements of VRR member boundaries are well constrained due to their long trace extents along both principal components and are consistent between studies, they are at odds with the interpretation of regional dips as flat (section 5) and with measurements of strata on member boundaries that do not uniformly dip northward. The discrepancy between regional bedding attitudes and orbiter-based measurements may indicate that features measured in HiRISE, which are mostly VRR member boundaries, do not represent primary bedding, and thus are discordant with strata. This discordancy could have multiple nonexclusive explanations: (1) the topographic ledges along each VRR member boundary could result from differential diagenesis (Fraeman et al., 2020), in which case the attitude of traces along the boundaries would not represent primary stratigraphy; (2) VRR member boundaries may have undergone significant postdepositional deformation that skewed their attitude from the primary regional structural orientation; (3) the members might retain lateral facies variations that change in elevation. In the first case, stratigraphic correlations between VRR members and Glen Torridon strata would be complicated by the possibility that VRR members are predominantly defined by diagenetic processes, in which case VRR members might not extend far south of the ridge despite regionally flat strata. In the second case, local deformation along the member boundaries could simultaneously explain steep dips of varying direction measured in situ on member boundaries and the fact that member boundaries do not follow elevation contours. In the third case, elevation variation along member boundaries could arise from primary processes such as deposition on preexisting lakebed topography in the form of low-relief depositional lobes, mounds, or channels. It is difficult to evaluate this scenario due to the limited spatial extent of rover observations. In addition to the aforementioned mechanisms, the attitudes of individual beds along the member contacts as measured in Mastcam images might be skewed toward the north relative to other outcrops on VRR due to downslope rotation, although this process would not bias orbiter-based measurements of the member boundaries. Other orbiter-based measurements of putative lower Mount Sharp strata (Table 2) are not necessarily subject to the same confounding conditions present on VRR, but measurements of VRR member attitudes highlight the possibility that orbital and in situ attitude measurements do not necessarily record the structural orientation of bedding.

5.3. Constraints on Stratigraphy of the Mount Sharp Group

In situ bed orientation measurements and regional stratigraphic correlations jointly constrain the geometry of strata and therefore the stratigraphic relationship between units in the Mount Sharp group. Figure 13 shows five notional stratigraphic models based on different scenarios for regional dips: 0° dip, 4°NW dip, 4°SE dip, 10°NW dip, and 10°SE dip. The 0° dip case (i.e., if the Mount Sharp group strata are flat) is supported by regional stratigraphic correlations (sections 4.1.1 and 4.1.2) and broadly consistent with the collection of individual and stacked bedding plane fits (sections 4.1 and 4.2). Under dip ~0°, the upper part of VRR is stratigraphically equivalent to the lower portions of Glen Torridon (Figure 13c). If contiguous, no BPm and few PPm strata would be expected to outcrop in Glen Torridon, although Jm strata would be expected to outcrop in the trough, which matches observations. Along the traverse in Figure 13a, VRR and Glen Torridon would be ~60 m and ~120 m thick, respectively. If dips are flat throughout the Mt Sharp group, the rover's elevation gain directly corresponds to the stratigraphic thickness of the traversed members.

A 4°NW dip and slightly shallower NW dips are more consistent with most orbiter-based dip measurements (Table 1, also see section 5.1) and some individual and stacked bed fits on VRR, especially those on the BPm-PPm contact (Table 1 and sections 4.1 and 4.2), but inconsistent with regional stratigraphic correlations and most stacked bed fits. In the 4°NW dip case, the upper BPm would be stratigraphically equivalent to Glen Torridon in most portions of the Glen Torridon trough and, because the dip would be close to the 5–6° regional slope, Glen Torridon would be thin (<20 m thick) relative to the overlying and underlying units. In this case, the BPm would outcrop in portions of the Glen Torridon trough, which is not observed. If the dip were 10°NW, which is inconsistent with all measurements, the conventional age relationship for the Mount Sharp group would reverse (strata would be older up section). A 4°SE dip and shallower SE dips is inconsistent with most in situ dip measurements and poorly supported by regional stratigraphic correlations. In the 4°SE dip case, the Jm would be stratigraphically equivalent to lower portions of Glen Torridon and units in the Mount Sharp group would have comparable thicknesses greater than those in the 0° dip case.

If the dip were 10°SE, which is inconsistent with all measurements, Glen Torridon and the sulfate-bearing (fractured-intermediate) unit would be stratigraphically thick compared to VRR.

5.4. Implications for Depositional Environment

Knowledge of the orientation of the Mount Sharp group also carries implications for understanding how sediment accumulation in Gale crater contributed to the formation of lower Mount Sharp. Mechanisms for mound formation that invoke erosion to present morphology may be supported by flat-lying or shallowly dipping strata (e.g., Andrews-Hanna et al., 2010; Day et al., 2016; Kite et al., 2013; Malin & Edgett, 2000), whereas if the mounds grew in place on preexisting topography (Kite et al., 2013, 2016), the constituent bedding should be closer to the regional dip.

The interpretation that dips within VRR and BPm are effectively flat supports the notion that, at least near the Glen Torridon region, strata were deposited horizontally on an equipotential surface or shallowly dipping and subsequently eroded to their present form (Grotzinger et al., 2015), and hence, the strata traversed by the Curiosity rover up through VRR did not directly contribute to the construction of Mount Sharp via anticompensational stacking. Even the steepest northward dips allowed by regional stratigraphic correlations (~2°NW, section 5) are significantly shallower than the 5–6° regional slope, requiring significant erosion to account for the discrepancy between the primary layer orientations and modern slope. This is consistent with the lacustrine hypothesis for accumulation of much of the Murray formation (Grotzinger et al., 2015; Fedo et al., 2017; Stack et al., 2019; Rivera-Hernandez et al., 2020). Flat dips in the Mount Sharp group do not necessarily dispute the possibility that the bulk of Mt Sharp formed by the accretion of draping strata in a mound shape (e.g., see hybrid model in Grotzinger et al., 2015, their Figure 8), as downslope layer orientation measurements in Gale crater are, with the exception of measurements on VRR in Fraeman et al., 2013, limited to the sulfate unit and above (Table 2; Kite et al., 2016). Anticompensational stacking is supported by many orbiter-based layer orientation measurements on sedimentary mounds, including in Gale crater above Glen Torridon, that show downslope bedding attitudes (Kite et al., 2016). Curiosity will eventually reach the sulfate-bearing unit where it can evaluate whether the layer orientations are consistent with anticompensational stacking, but quantitative rover-based assessments of layer orientations above Glen Torridon are not yet possible.

6. Conclusions and Imaging Recommendations

We have presented the first in situ constraints on the orientation of Mount Sharp group strata using a combination of measurements made from stereo Mastcam images and regional stratigraphic correlations. Bed orientations were measured in the Blunts Point, Pettegrove Point, and Jura members of the Murray formation. We implemented the PCA-based analytical approach of Quinn and Ehlmann (2019b) in conjunction a Monte Carlo bootstrapping technique to account for nonuniform stereo errors and a variance-based framework for computing statistically based stereo errors. Even in with relatively low plane fit uncertainty, true variations in strata orientation, likely predominantly due to postdepositional rotation or deformation (e.g., impact cratering), make it difficult to tightly constrain regional orientations by averaging the attitudes of bedding measured in situ at different sites. In situ measurements constrain regional attitudes to be within several degrees of horizontal. Regional stratigraphic correlations of rock targets within the so-called "Flodigarry facies," a package of rocks at the base of the Pettegrove Point-Jura Member contact, constrain dips to be between ~3°SE and 2°NW regionally. The absence of lithologies matching the Pettegrove Point member within the areas of Glen Torridon explored thus far by the Curiosity rover constrains dips to be no more than a few degrees NW or indicates that the strata are unrecognizable or laterally discontinuous. As the rover continues its traverse through Glen Torridon, the identification or absence of lithologies matching the Blunts Point member may further constrain regional structural orientation, as its presence in Glen Torridon would suggest dips are regionally higher than we predict.

Overall, the results of this study suggest that the strata comprising the Blunts Point, Pettegrove Point, and Jura members are approximately horizontal, consistent with sediment deposition on a flat, equipotential surface. At least part of the Glen Torridon trough is stratigraphically equivalent to the Jura member of VRR. There is a discrepancy between the orientation of VRR member boundaries as measured from HiRISE, where they dip ~6–7°N, and the dip constraints in this study, indicating that the member boundaries and the strata that comprise them are discordant. This discordancy may arise from the possibility

that VRR members are distinguished primarily by diagenetic processes that did not follow strata boundaries, in which case stratigraphic correlations between VRR members and strata in the Glen Torridon trough must be treated cautiously, as member correlations and stratigraphic correlations may differ.

This study also highlights potential improvements to imaging strategies that could benefit MSL, Mars2020, and future rover missions with stereo imaging capabilities. The greatest challenge in deriving accurate rover-based attitude measurements, apart from confidence that the observed orientations are primary, is the poor ratio of plane extent (described by the $\bar{x}_1 - \bar{x}_2$ plane) to the error in the plane fit $\bar{x}_3$, which results from a combination of limited outcrop exposure and the small stereo baseline of the Mastcams and Navcams. Even scenes with relatively long bedding exposures can yield highly uncertain fits if traces fall predominantly along a single principal component axis. The uncertainty of plane solutions can be improved by shortening the distance to targets to reduce the range error (typically to distances of less than 10 m), stacking multiple bed traces from a single scene to increase the sampling extent in the $\bar{x}_1 - \bar{x}_2$ plane, or collecting stereo images of the same target from multiple positions (i.e., multiple baseline stereo imaging).

As Curiosity continues its traverse of Glen Torridon, we expect that the methods described here will be utilized to validate the interpretation of the regional structural orientation of the Mount Sharp group as flat, and eventually to characterize the orientation of layers in the sulfate-bearing strata.

Acknowledgments
Mastcam images presented in this paper are archived in the Planetary Data System (pds.nasa.gov). Archives of all Mastcam stereo products will be available via the NASA Planetary Data System (PDS) through the Mastcam Stereo Analysis and Mosaics (MSAM) project (Deen et al., 2019). All derived bed trace products are archived at CaltechDATA (doi:10.22002/D1.1318). The software used to fit bedding planes is archived at CaltechDATA (Attitude, doi:10.22002/D1.1211, https://data.caltech.edu/records/1211). We are grateful to the Mars Science Laboratory Project engineering and science teams, as well as MSL team members who participated in tactical and strategic operations, for their diligent efforts required to collect the data presented here. Thanks to the MSL sed-strat working group, Kevin Lewis, Maddie Turner, and Edwin Kite for their input that improved the material presented in this manuscript. We also thank David Rubin and an anonymous reviewer for their input. B. L. E. acknowledges support from the MSL Participating Scientist Program. A portion of this research was carried out at the Jet Propulsion Laboratory, California Institute of Technology, under a contract with the National Aeronautics and Space Administration.

References

Abarca, H., Deen, R., Hollins, G., Zamani, P., Maki, J., Tinio, A., et al. (2019). Image and data processing for InSight lander operations and science. *Space Science Reviews*, *215*(2), 1–53. https://doi.org/10.1007/s11214-019-0587-9

Alexander, D. & Deen, R. (2017). Mars Science Laboratory project software interface specification (SIS); camera & LIBS experiment data record (EDR) and reduced data record (RDR) data products, version 4.0. JPL doc. D-38107, data set MSL-M-NAVCAM-2-EDR-V1.0, NASA planetary data system.

Andrews-Hanna, J. C., Zuber, M. T., Arvidson, R. E., & Wiseman, S. M. (2010). Early Mars hydrology: Meridiani playa deposits and the sedimentary record of Arabia Terra. *Journal of Geophysical Research*, *115*, E06002. https://doi.org/10.1029/2009je003485

Arvidson, R. E., Ashley, J. W., Bell, J. F. III, Chojnacki, M., Cohen, J., Economou, T. E., et al. (2011). Opportunity Mars Rover mission: Overview and selected results from Purgatory ripple to traverses to Endeavour crater. *Journal of Geophysical Research*, *116*, E00F15. https://doi.org/10.1029/2010JE003746

Banham, S. G., Gupta, S., Rubin, D. M., Watkins, J. A., Sumner, D. Y., Edgett, K. S., et al. (2018). Ancient Martian aeolian processes and palaeomorphology reconstructed from the Stimson formation on the lower slope of Aeolis Mons, Gale crater, Mars. *Sedimentology*, *65*(4), 993–1042. https://doi.org/10.1111/sed.12469

Barnes, R., Gupta, S., Traxler, C., Ortner, T., Bauer, A., Hesina, G., et al. (2018). Geological analysis of Martian rover-derived digital outcrop models using the 3-D visualization tool, planetary robotics 3-D viewer—Pro3D. *Journal of Geophysical Research, Planets*, *5*, 285–307. https://doi.org/10.1002/2018EA000374

Bell, J. F. III, Godber, A., McNair, S., Caplinger, M. A., Maki, J. N., Lemmon, M. T., et al. (2017). The Mars Science Laboratory Curiosity rover Mastcam instruments: Preflight and in-flight calibration, validation, and data archiving. *Earth and Space Science*, *4*, 396–452. https://doi.org/10.1002/2016EA000219

Bennett, K., Fox, V. K., Bryk, A. B., Fedo, C., Vasavada, A. R., Dehouck, E., et al. (2019). Results from the Curiosity rover's traverse through the clay-bearing Glen Torridon region in Gale crater. *AGU Fall Meeting*. P33B-01.

Bennett, K., Rivera-Hernandez, F., Tinker, C., Horgan, B., Fey, D. M., Edwards, C., et al. (2020). MAHLI at Vera Rubin ridge, Gale crater, Mars: Fine-scale features reveal extensive diagenesis. *Journal of Geophysical Research*. This special issue.

Day, M., & Kocurek, G. (2016). Observations of an aeolian landscape: From surface to orbit in Gale Crater. *Icarus*, *280*, 37–71. https://doi.org/10.1016/j.icarus.2015.09.042

Deen, R., Zamani, P., Abarca, H., Maki, J. (2019). InSight project software interface specification (SIS); Camera experiment data record (EDR) and reduced data record (RDR) data products. v.3.3. JPL D-56937. NASA Planetary Data System.

DiBiase, R. A., Limaye, A. B., Scheingross, J. S., Fischer, W. W., & Lamb, M. P. (2013). Deltaic deposits at Aeolis Dorsa: Sedimentary evidence for a standing body of water on the northern plains of Mars. *Journal of Geophysical Research*, *118*, 1285–1302. https://doi.org/10.1002/jgre.20100

Edgar, L., Fedo, C. M., Gupta, S., Banham, S. G., Fraeman, A. A., Grotzinger, J. P., et al. (2020). A lacustrine paleoenvironment recorded at Vera Rubin Ridge, Gale crater: Overview of the sedimentology and stratigraphy observed by the Mars Science Laboratory Curiosity rover. *Journal of Geophysical Research, Planets*, *125*, e2019JE006307. https://doi.org/10.1029/2019JE006307

Edgar, L. A., Gupta, S., Rubin, D. M., Lewis, K. W., Kocurek, G. A., Anderson, R. B., et al. (2017). Shaler: A fluvial sedimentary deposit on Mars. *Sedimentology*, *65*(1), 96–122. https://doi.org/10.1111/sed.12370

Fedo, C., Fedo, C., Grotzinger, J. P., Edgar, L. A., Fox, V. K., Bennett, K. A., et al.(2019). Connecting lower Mount Sharp strata: How does the clay-bearing unit in Glen Torridon relate to the Murray formation, Gale crater, Mars. *AGU Fall Meeting*. P31A-3422.

Fedo, C., Grotzinger, J.P., Bryk, A., Edgar, L. A., Bennett, K., Fox, K., et al. (2020). Ground-based stratigraphic correlation of the Jura and Knockfarril Hill members of the Murray formation, Gale crater: Bridging the Vera Rubin ridge-Glen Torridon divide. *LPSC 51*. Abstract 2345.

Fedo, C., Grotzinger, J. P., Gupta, S., Fraeman, A., Edgar, L., Edgett, K., et al. (2018). Sedimentology and stratigraphy of the Murray formation, Gale Crater, Mars. *LPSC 49*. Abstract 2078.

Fox, V., Bennett, K. A., Bristow, T., Ehlmann, B., House, C., Fairén, A. G., et al. & the MSL Science Tea (2019). Exploring the clay-bearing unit with the Curiosity rover. *LPSC* 50. Abstract 2826.

Fraeman, A. A., Edgar, L. A., Rampe, E. B., Thompson, L., Frydenvang, J., Bryk, A., Fedo, C. M., et al. (2020). The origin of Vera Rubin ridge: Overview and results from Curiosity's exploration campaign. *This special issue*.

Fraeman, A. A., Arvidson, R. E., Catalano, J. G., Grotzinger, J. P., Morris, R. V., Murchie, S. L., et al. (2013). A hematite-bearing layer in Gale Crater, Mars: Mapping and implications for past aqueous conditions. *Geology*, *41*(10). https://doi.org/10.1130/G34613.1

Fraeman, A. A., Ehlmann, B. L., Arvidson, R. E., Edwards, C. S., Grotzinger, J. P., Milliken, R. E., et al. (2016). The stratigraphy and evolution of lower Mount Sharp from spectral, morphological, and thermophysical orbital data sets. *Journal of Geophysical Research, Planets*, *121*, 1713–1736. https://doi.org/10.1002/2016JE005095

Fueten, F., Stesky, R. M., & MacKinnon, P. (2005). Structural attitudes of large scale layering in Valles Marineris, Mars, calculated from Mars Orbiter Laser Altimeter data and Mars Orbiter camera imagery. *Icarus*, *175*(1). https://doi.org/10.1016/j.icarus.2004.11.010

Goudge, T. A., Milliken, R. E., Head, J. W., Mustard, J. F., & Fassett, C. I. (2017). Sedimentological evidence for a deltaic origin of the western fan deposit in Jezero crater, Mars and implications for future exploration. *Earth and Planetary Science Letters*, *458*. https://doi.org/10.1016/j.epsl.2016.10.056

Grotzinger, J. P., Gupta, S., Malin, M. C., Rubin, D. M., Schieber, J., Siebach, K., et al. (2015). Deposition, exhumation, and paleoclimate of an ancient lake deposit, Gale crater, Mars. *Science*, *350*(6257). https://doi.org/10.1126/science.aac7575

Grotzinger, J. P, & Milliken, R. (2012). The sedimentary rock record of Mars: Distribution, origins, and global stratigraphy. In J. P. Grotzinger & R. Milliken (Eds.), *Sedimentary geology of Mars* (Vol. 102, pp. 1–48). Tulsa, OK: SEPM.

Grotzinger, J. P., Sumner, D. Y., Kah, L. C., Stack, K., Gupta, S., Edgar, L., et al., & MSL Science Team (2014). A habitable fluvio-lacustrine environment at Yellowknife Bay, Gale Crater, Mars. *Science*, *343*(6169), 1242777. https://doi.org/10.1126/science.1242777

Gwizd, S., Fedo, C., Grotzinger, J., Edgett, K., Rivera-Hernandez, F., Stein, N. (2019). Depositional history of the Hartmann's Valley member, Murray formation, Gale crater, Mars. *LPSC 49*. Abstract 2150.

Hayes, A. G., Grotzinger, J. P., Edgar, L. A., Squyres, S. W., Watters, W. A., & Sohl-Dickstein, J. (2011). Reconstruction of eolian bed forms and paleocurrents from cross-bedded strata at Victoria Crater, Meridiani Plaum, Mars. *Journal of Geophysical Research*, *116*, E00F21. https://doi.org/10.1029/2010JE003688

Hurowitz, J. A., Grotzinger, J. P., Fischer, W. W., McLennan, S., Milliken, R. E., Stein, N., et al. (2017). Redox stratification of an ancient lake in Gale crater, Mars. *Science*, *356*(6341). https://doi.org/10.1126/science.aah6849

Hynek, B. M., & Phillips, R. J. (2008). The stratigraphy of Meridiani Planum, Mars, and implications for the layered deposits' origin. *Earth and Planetary Science Letters*, *274*(1–2). https://doi.org/10.1016/j.epsl.2008.07.025

Kite, E. S., Lewis, K. W., Lamb, M. P., Newman, C. E., & Richardson, M. I. (2013). Growth and form of the mound in Gale Crater, Mars: Slope wind enhanced erosion and transport. *Geology*, *41*(5). https://doi.org/10.1130/G33909.1

Kite, E. S., Sneed, J., Mayer, D. P., Lewis, K. W., Michaels, T. I., Hore, A., & Radkin, S. C. R. (2016). Evolution of major sedimentary mounds on Mars: Buildup via anticompensational stacking modulated by climate change. *Journal of Geophysical Research, Planets*, *121*, 2282–2324. https://doi.org/10.1002/2016JE005135

Le Deit, L., Hauber, E., Fueten, F., Pondrelli, M., Pio Rossi, A., & Jaumann, R. (2013). Sequence of infilling events in Gale Crater, Mars: Results from morphology, stratigraphy, and mineralogy. *Journal of Geophysical Research, Planets*, *118*, 2439–2473. https://doi.org/10.1002/2012JE004322

Lewis, K. W., & Aharonson, O. (2006). Stratigraphic analysis of the distributary fan in Eberswalde crater using stereo imagery. *Journal of Geophysical Research*, *111*, E06001. https://doi.org/10.1029/2005JE002558

Lewis, K. W., & Aharonson, O. (2014). Occurrence and origin of rhythmic sedimentary rocks on Mars. *Journal of Geophysical Research, Planets*, *119*, 1432–1457. https://doi.org/10.1002/2013JE004404

Lewis, K. W., Aharonson, O., Grotzinger, J. P., Kirk, R. L., McEwen, A. S., & Suer, T. A. (2008). Quasi-periodic bedding in the sedimentary rock record of Mars. *Science*, *322*(1532). https://doi.org/10.1126/science.1161870

Lewis, K. W., Aharonson, O., Grozinger, J. P., Squyres, S. W., Bell, J. F., Crumpler, L. S., & Schmidt, M. E. (2008). Structure and stratigraphy of home plate from the Spirit Mars exploration rover. *Journal of Geophysical Research*, *113*, E12S36. https://doi.org/10.1029/2007JE003025

Lewis, K.W. and Turner, M.L. (2019). Geologic structure of the Vera Rubin Ridge, Gale Crater, Mars. *LPSC 50*. Abstract 2216.

Lewis, K.W., Turner, M.L., and Stack, K.M. (2020). Implications of non-horizontal stratigraphy at Mount Sharp, Gale Crater, Mars. *LPSC 51*. Abstract 2544.

Maki, J., Thiessen, D., Pourangi, A., Kobzeff, P., Litwin, T., Scherr, L., et al. (2012). The Mars Science Laboratory engineering cameras. *Space Science Reviews*, *170*(1-4), 77–93. https://doi.org/10.1007/s11214-012-9882-4

Malin, M. C., & Edgett, K. S. (2000). Sedimentary rocks of early Mars. *Science*, *290*, 1927–1937. https://doi.org/10.1126/science.290.5498.1927

Malin, M. C., Ravine, M. A., Caplinger, M. A., Shaemi, F. T., Schaffner, J. A., Maki, J. N., et al. (2017). The Mars Science Laboratory (MSL) Mast cameras and descent imager: I. Investigation and instrument descriptions. *Earth and Space Science*, *4*, 506–539. https://doi.org/10.1002/2016EA000252

Metz, J., Grotzinger, J., Okubo, C., & Milliken, R. (2010). Thin-skinned deformation of sedimentary rocks in Valles Marineris, Mars. *Journal of Geophysical Research*, *115*, E11004. https://doi.org/10.1029/2010JE003593

Milliken, R. E., Grotzinger, J. P., & Thomson, B. J. (2010). Paleoclimate of Mars as captured by the stratigraphic record in Gale Crater. *Geophysical Research Letters*, *37*, L04201. https://doi.org/10.1029/2009GL041870

Minitti, M. E., Malin, M. C., van Beek, J. K., Caplinger, M., Maki, J. N., Ravine, M., et al. (2019). Distribution of primary and secondary features in the Pahrump Hills outcrop (Gale crater, Mars) as seen in a Mars Descent Imager (MARDI) "sidewalk" mosaic. *Icarus*, *328*, 194–209. https://doi.org/10.1016/j.icarus.2019.03.005

Okubo, C. H. (2010). Structural geology of Amazonian-aged layered sedimentary deposits in southwest Candor Chasma, Mars. *Icarus*, *207*(1). https://doi.org/10.1016/j.icarus.2009.11.012

Okubo, C. H., Lewis, K. W., McEwen, A. S., & Kirk, R. L. (2008). Relative age of interior layered deposits in southwest Candor Chasma based on high-resolution structural mapping. *Journal of Geophysical Research*, *113*, E12002. https://doi.org/10.1029/2008JE003181

Quinn, D. P., & Ehlmann, B. L. (2019a). The deposition and alteration history of the northeast Syrtis Major layered sulfates. *Journal of Geophysical Research, Planets*, *124*, 1743–1782. https://doi.org/10.1029/2018JE005706

Quinn, D. P., & Ehlmann, B. L. (2019b). A PCA-based framework for determining remotely sensed geological surface orientations and their statistical quality. *Earth and Space Science*, *6*, 1378–1408. https://doi.org/10.1029/2018EA000416

Rapin, W., Ehlmann, B. L., Dromart, G., Schieber, J., Thomas, N. H., Fischer, W. W., et al. (2019). An interval of high salinity in ancient Gale crater lake on Mars. *Nature Geoscience*, *12*(11), 889–895. https://doi.org/10.1038/s41561-019-0458-8

Rivera-Hernandez, F., Sumner, D. Y., Mangold, N., Stack, K. M., Forni, O., Newsom, H., et al. (2019). Using ChemCam LIBS data to constrain grain size in rocks on Mars: Proof of concept and application to rocks at Yellowknife Bay and Pahrump Hills, Gale crater. *Icarus*, *321*, 82–98. https://doi.org/10.1016/j.icarus.2018.10.023

Rivera-Hernandez, F., Sumner, D. Y., Mangold, N., Banham, S. G., Edgett, K. S., Fedo, C. M., et al. (2020). Grain size variations in the Murray formation: Stratigraphicevidence for changing depositional environments in Gale crater, Mars. *Journal of Geophysical Research, Planets*, *125*, e2019JE006230. https://doi.org/10.1029/2019/JE006230

Rubin, D.M. & Carter, C.L. (2006). Bedforms and cross-bedding in animation: Society for Sedimentary Geology (SEPM) Atlas Series.

Siebach, K. L., Fedo, C. M., Edgar, L. E., Edgett, K., Grotzinger, J. P., Fraeman, A. A., et al. (2019). *Overview of Gale crater stratigraphy and sedimentology from 6 years of roving with Mars Science Laboratory*. LPSC 50. Abstract 2132.

Squyres, S. W., Grotzinger, J. P., Arvidson, R. E., Bell, J. F. III, Calvin, W., Christensen, P. R., et al. (2004). In situ evidence for an ancient aqueous environment at Meridiani*Planum, Mars. Science*, *306*(5702), 1709–1714. https://doi.org/10.1126/science.1104559

Stack, K. E., Sun, V. Z., Arvidson, R. E., Fedo, C., Day, M., Bennett, K., et al. (2019). Origin of linear ridges in the clay-bearing unit of Mount Sharp, Gale Crater, Mars. *LPSC 50*. Abstract 1210.

Stack, K. M., Cofield, S. M., & Fraeman, A. A. (2017). Geologic map of the MSL Curiosity rover extended mission traverse of Aeolis Mons, Gale Crater, Mars. *LPSC 48*. Abstract 1889.

Stack, K. M., Grotzinger, J. P., & Milliken, R. E. (2013). Bed thickness distributions on Mars: An orbital perspective. *Journal of Geophysical Research, Planets*, *118*, 1323–1349. https://doi.org/10.1002/jgre.20092

Stein, N., Grotzinger, J. P., Schieber, J., Mangold, N., Hallet, B., Newsom, H., et al. (2018). Desiccation cracks provide evidence of lake drying on Mars, Sutton Island member, Murray formation, Gale Crater. *Geology*, *46*(6), 515–518. https://doi.org/10.1130/G40005.1

Turner, M.L. & Lewis, K.W. (2019). Geologic structure of the Vera Rubin ridge and clay-bearing Glen Torridon region, Gale crater, Mars. *AGU Fall Meeting*. P31A-3424.

Watters, W. A., Grotzinger, J. P., Bell, J., Grant, J., Hayes, A. G., Li, R., et al. (2011). Origin of the structure and planform of small impact craters in fractured targets: Endurance crater at Meridiani Planum, Mars. *Icarus*, *211*(1). https://doi.org/10.1016/j.icarus.2010.08.030

Williams, R. M. E., Grotzinger, J. P., Dietrich, W. E., Gupta, S., Sumner, D. Y., Wiens, R. C., et al. (2013). Martial fluvial conglomerates at Gale Crater. *Science*, *340*(6136), 1068–1072. https://doi.org/10.1126/science.1237317